

Chapter 4 Persistence Length Study of Protein Nanotubes

From Chapter 4 to Chapter 6, I will present the different approaches which were employed to access the physical properties of protein nanotubes using AFM. In this chapter, a persistence length method will be applied on three different nanotubes. Persistence length is a mechanical property quantifying the flexibility of a filament, in this case a protein nanotube, which provides an indication of how much a filament “persists” in its initial orientation. Associating the geometry of the cross section of the filament studied, the elasticity of the filament is also able to be estimated.

4.1 Theory and Method

4.1.1 Persistence Length is a Measure of the Flexibility of a Filament

The definition of persistence length is “the average projection of the end-to-end vector on the tangent to the chain contour at a chain end in the limit of infinite chain length” (IUPAC Gold Book). Considering a filament as succession of segment vectors of length l , as demonstrated in **Figure 4-1**, the angle between the end-to-end vector from position 0 to position 1 and the tangent vector at position 0 is θ . The projection of the end-to-end vector on the tangent vector is $l\cos\theta$. The average of this projection is $l\langle\cos\theta\rangle$ ($\langle\rangle$ denotes the average). If the contour

length of the filament becomes sufficiently long, consequently the number of segments becomes sufficiently large, the average projection approaches a constant value, which is termed the persistence length P (Equation 4-1).

$$\langle \cos \theta \rangle = e^{-(l/P)}$$

Equation 4-1

In other words, the persistence length is the length over which correlations in the segment directions are lost. The expectation value of the cosine of the angle falls off exponentially with distance. A more detailed explanation of persistence length can be found in Frontali's (1979) and Hagerman's (1988) work.

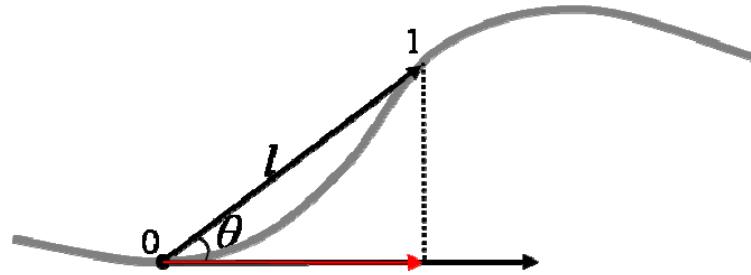


Figure 4-1 A sketch of a thin flexible filament. The segment vector from position 0 to position 1, the tangent vector at position 0, and the angle θ between these two vectors are shown. The projection of the segment vector on the tangent vector is shown by a red arrow.

Persistence length is independent of the contour length of the filament (Hagerman, 1988). However, the persistence length is related to the end-to-end distance of the filament. The relation between the mean-square end-to-end distance R and the persistence length P is given by Equation 4-2 (Flory 1969; Rivetti *et al.* 1996).

$$\langle R^2 \rangle = 4Ps \left[1 - \frac{2P}{s} (1 - e^{-s/2P}) \right]$$

Equation 4-2

where s is the contour length of the filament.

The persistence length is a measure of the flexibility of a filament. The higher the persistence length, the more rigid the filament; the lower the persistence length, the more flexible it is. The flexibility of a filament is related to its elasticity through **Equation 4-3** (Landau and Lifshitz 1980; 1986).

$$EI = k_B TP$$

Equation 4-3

where E is the Young's modulus, I is the area moment of inertia of the cross section of the filament ($I = \pi D^4/64$, for a circular area with diameter D), k_B is the Boltzmann constant and T is the absolute temperature. If the persistence length of the filament can be obtained from AFM images, together with the geometry of the cross section, the Young's modulus can therefore be estimated.

4.1.2 Analysing AFM Images of Nanofibrils and Nanotubes to Obtain Their Persistence Lengths

AFM images of nanofibrils or nanotubes were analysed using Veca, an image processing software developed by A. Orta (LBSA, University of Nottingham, UK). The analysis process is as follows:

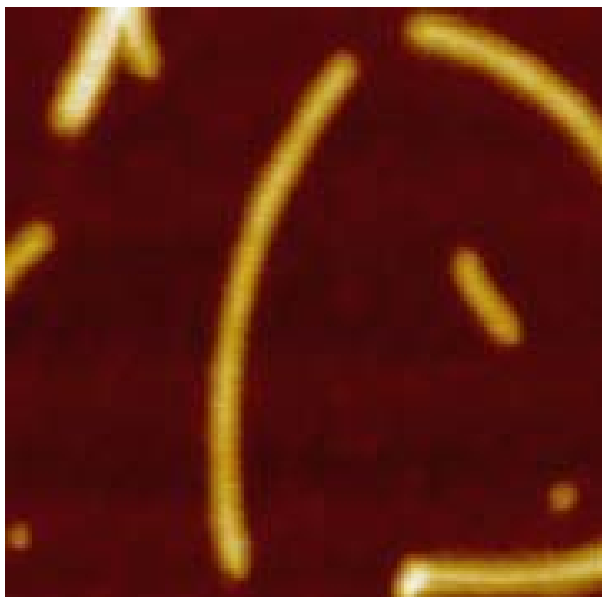


Figure 4-2 An AFM tapping mode height image of *Salmonella* flagellar filaments observed on mica in air. The size of the image is $1\mu\text{m}\times 1\mu\text{m}$. The filament of interest is the long filament lying approximately vertically on the middle of this image.

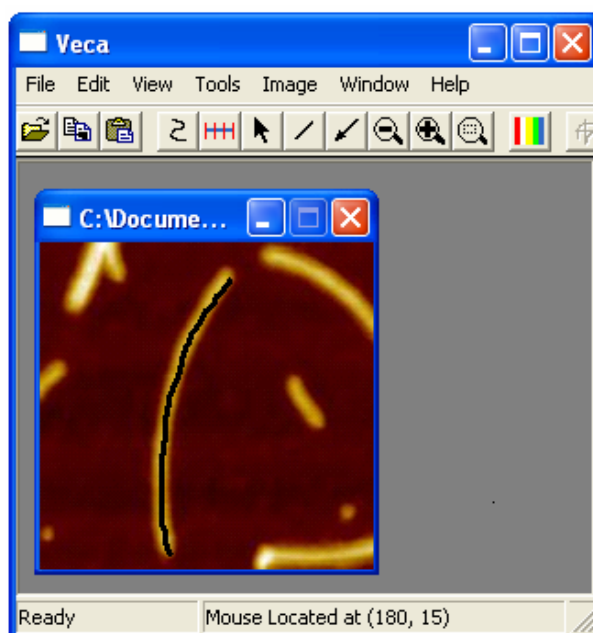


Figure 4-3 Use of “Freehand” tool to trace the contour of a filament within Veka. The layout of Veka is shown. The AFM image of **Figure 4-2** is open inside of Veka. The black line along the filament is the trace line drawn with the mouse using the “Freehand” tool of Veka.

First, AFM height images were exported from SPIP software (**Figure 4-2**) (see section 2.1.3 for the details of using SPIP software). After calibration of the scale, the contours of nanofibrils or nanotubes were traced using the “Freehand” tool within the Veca software. The layout of Veca is displayed in **Figure 4-3**.

Second, the contour of the filament then was digitalised and recorded as a set of XY-coordinate by Veca. In order to minimise experimental data acquisition errors, a smoothing procedure using the weighted average of five contiguous XY-coordinates centred about a given XY-coordinate was performed (Mucke *et al.* 2004).

$$V_{i,correct} = \frac{1V_{i-2} + 2V_{i-1} + 4V_i + 2V_{i+1} + 1V_{i+2}}{10}$$

Equation 4-4

where V_i is the vector of the tangent to the curve on XY-coordinate i . This procedure removes two points at each end of the filament. The smoothed XY-coordinates of the filament shown in **Figure 4-2** are displayed in **Figure 4-4**.

Third, **Equation 4-1** or **Equation 4-2** was used to compute the persistence length. If **Equation 4-1** was used, the filament contour was split into segments of increasing segment length l , and for each set of segment length, the mean cosine angle $\langle \cos \theta \rangle$ and the persistence length P calculated. The persistence length was then plotted as a function of contour segment length l (**Figure 4-5**). A clear maximum value of persistence length P_0 was discerned using this method, which corresponding to the value of the persistence length of the filament.

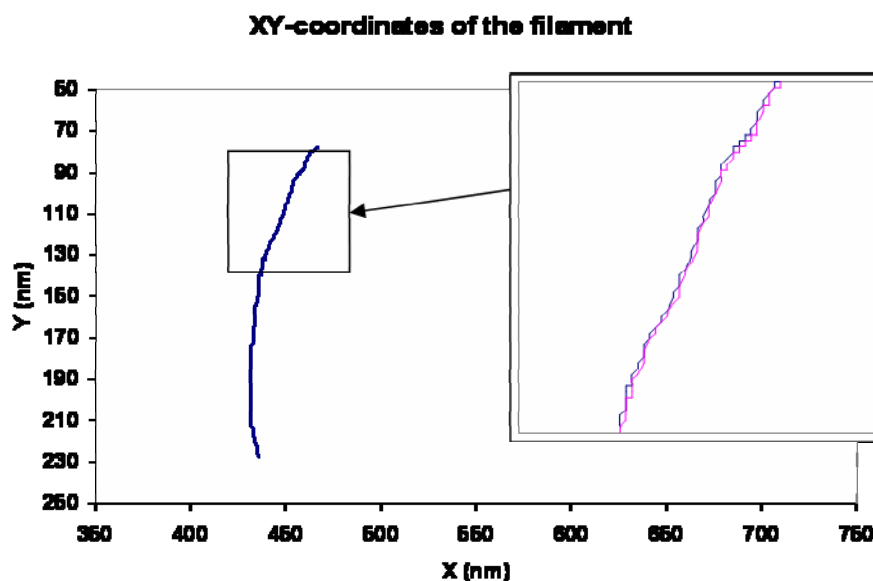


Figure 4-4 The contour of the filament shown in **Figure 4-2** is digitalised to XY-coordinate sets here. The blue curve is plotted with smoothed XY-coordinates. The part enclosed by the square is enlarged and shown on the inset. The pink curve on the inset is plotted with the original XY-coordinates before smoothing.

As shown in **Figure 4-5**, the value of persistence length typically was found to decrease at lower and higher contour segment length l . At lower l , the discretization during data processing results in an underestimation of persistence length. At higher l , the small angles are overlooked; therefore the number of small angles is undercounted, which leads to underestimation of persistence length as well.

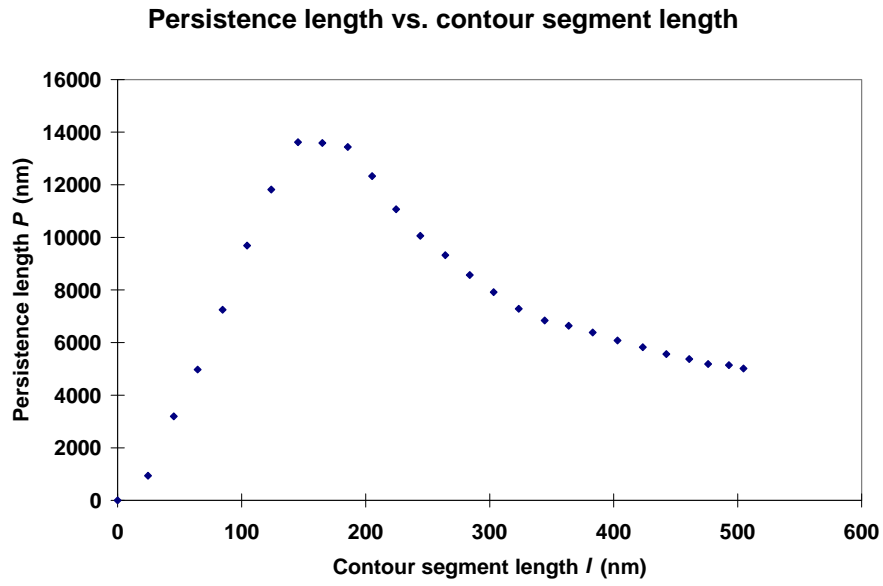


Figure 4-5 Persistence length P against contour segment length l . A peak value of persistence length $P_0 = 13.6 \mu\text{m}$ in the range $l = 120$ nm to 200 nm can be discerned, which is the value of persistence length of the filament shown on **Figure 4-2**.

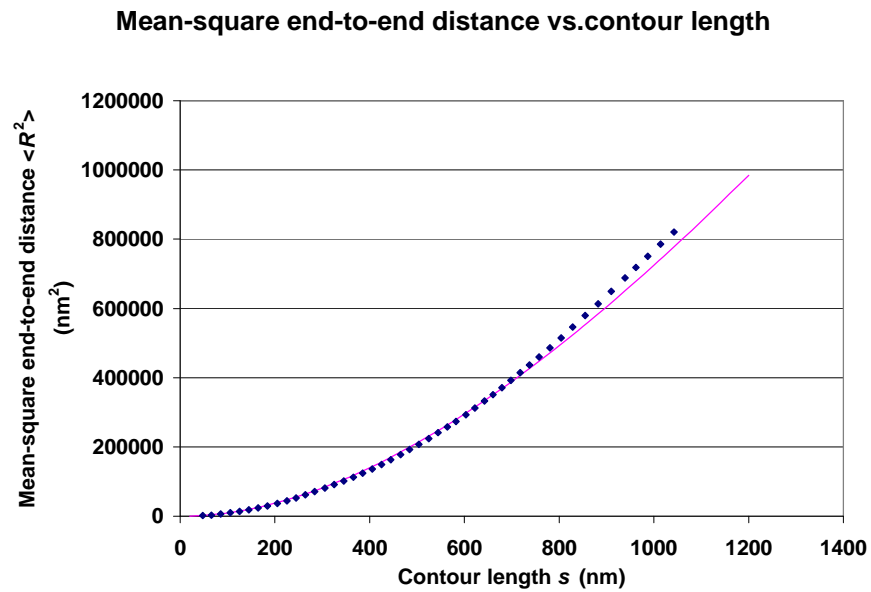


Figure 4-6 The plot of the mean square end-to-end distance $\langle R^2 \rangle$ against the contour length s of the filament on **Figure 4-2**. The pink line is the fitted curve using the Levenberg-Marquardt algorithm (Press *et al.* 1992). The persistence length computed for this filament is $P_R = 474$ nm.

If **Equation 4-2** was used, the filament was split into segments of increasing contour length s , and for each set of contour lengths, the mean-square end-to-end distance $\langle R^2 \rangle$ calculated. The mean-square end-to-end distance was then plotted against the contour length s . The experimental data then is fitted into **Equation 4-3** to obtain the persistence length P_R , using the Levenberg-Marquardt algorithm (Press *et al.* 1992).

4.2 The Persistence Length of Flagellar Filaments in Different Environments

As discussed in section 3.1, *Salmonella* flagellar filaments were imaged under different conditions in order to investigate the effects of the environment on their structures. Here, in order to investigate the environmental effect on their elastic properties, the topography images obtained in section 3.1 (e.g. **Figure 3-1**, **Figure 3-10** and **Figure 3-11**) were used to compute the persistence length.

Although images of *Salmonella* flagellar filaments on mica in aqueous environments have been obtained, imaging in aqueous environments is difficult to operate and time consuming. As bulk data was needed for persistence length calculation, images of *Salmonella* flagellar filaments on mica in air (see section 3.1.1) were used to obtain persistence length. The limited on mica in liquid images obtained (see section 3.1.2) agreed with the on mica in air persistence length results.

A typical data analysis of a *Salmonella* flagellar filament obtained by applying **Equation 4-1** is displayed in **Figure 4-5**. The peak values of persistence length obtained in my experiments lied between $l = 100$ nm to 200 nm. As explained

above (section 4.1), underestimation of persistence length at lower l values is expected. Therefore only filaments with contour length longer than 400 nm were selected for measuring persistence length. This selection rule also had an advantage of giving a clear peak value of persistence length in the chart of persistence length versus contour segment length. The persistence length of *Salmonella* flagellar filaments on mica in air obtained was $P_0 = 11 \pm 2 \mu\text{m}$.

A typical data analysis of a *Salmonella* flagellar filament through the application of Equation 4-2 is displayed in Figure 4-6. The persistence length of *Salmonella* flagellar filaments on mica in air was found to be $P_R = 0.46 \pm 0.08 \mu\text{m}$. The distribution of P_R is displayed in Figure 4-7.

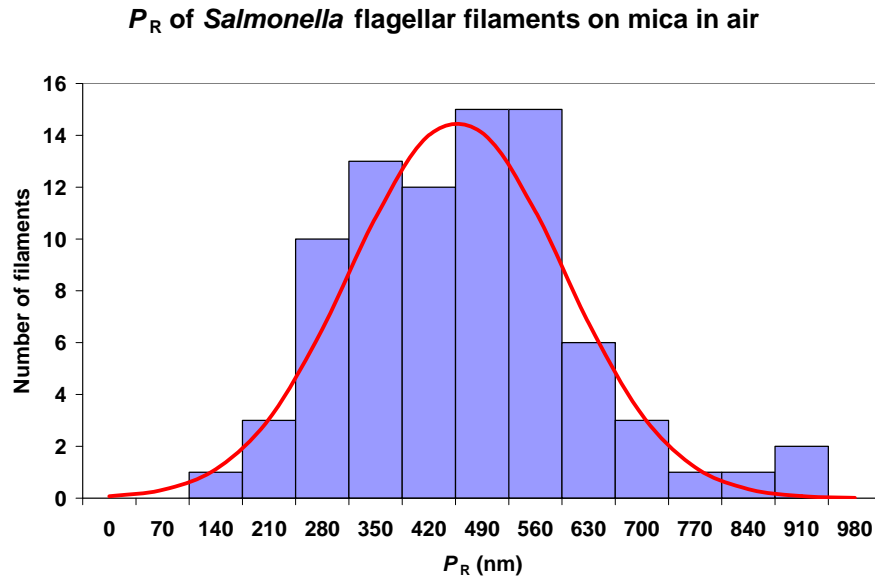


Figure 4-7 Histogram of the persistence length obtained for *Salmonella* flagellar filaments on mica in air through the application of Equation 4-2. The mean persistence length measured was found to be $P_R = 0.46 \pm 0.08 \mu\text{m}$ ($N = 82$).

The topography images of *Salmonella* flagellar filaments on gold in air and in propanol-water (80:20) mixture obtained in section 3.1.3 were also used to compute persistence length.

Salmonella flagellar filaments were found to be broken over the gaps between the gold islands of gold substrates (indicated by a blue arrow in **Figure 4-8** (left)). This is most likely due to the drying process during sample preparation, and/or by the force applied by the AFM probe during scanning. The two pink arrows in **Figure 4-8** (left) indicate the ends of two filaments which lie down over the edge of a gold island. This can be observed more clearly in the 3D picture (**Figure 4-8** (right), also indicated by two pink arrows). In addition to the selection rule described above, which was employed to select the filaments with contour lengths over 400 nm, another selection rule was applied for on gold analysis, which was that only those filaments or part of the filaments lying upon one plateau were selected for measurement persistence length.

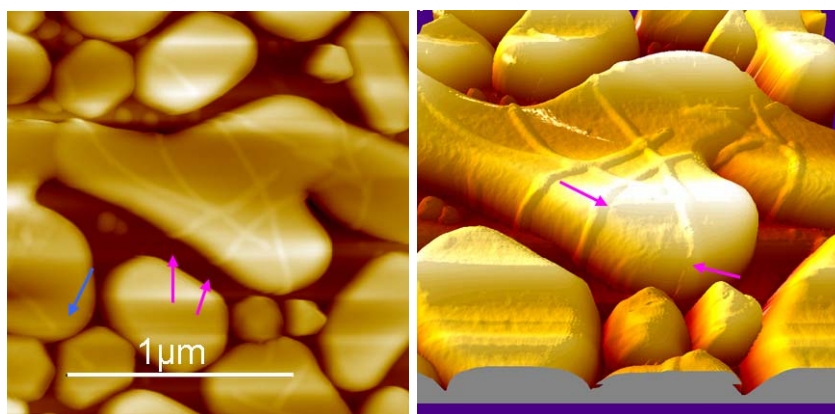


Figure 4-8 Tapping mode AFM height image of *Salmonella* flagellar filaments in air on gold. The right picture is a 3-D picture of the left image generated by SPIP software. Stock sample solutions were 100 times diluted. The Z-scale is 240.0 nm.

In a similar manner, the persistence length for *Salmonella* flagellar filaments on gold in air was found to be $P_{\theta} = 13 \pm 3 \text{ } \mu\text{m}$ and $P_R = 0.20 \pm 0.05 \text{ } \mu\text{m}$. The persistence length of the *Salmonella* flagellar filaments imaged on gold in propanol-water (80:20) mixture were found to be $P_{\theta} = 4.1 \pm 0.4 \text{ } \mu\text{m}$ and $P_R = 0.19 \pm 0.04 \text{ } \mu\text{m}$.

The average persistence lengths (P_R , P_{θ}) of *Salmonella* flagellar filaments on mica and gold in air, and on gold in propanol-water mixture are displayed in **Table 4-1**.

Table 4-1 *Salmonella* flagellar filaments in different environments.

Environment		On mica	On gold	
		In air	In air	In 80% propanol
Persistence length	$P_R \text{ (}\mu\text{m)}$	0.46 ± 0.08	0.20 ± 0.05	0.19 ± 0.04
	$P_{\theta} \text{ (}\mu\text{m)}$	11 ± 2	13 ± 3	4.1 ± 0.4
P_R / P_{θ}		4.2%	1.5%	4.6%

AFM images of the filaments showed the contour of the filaments transformed from three dimensional (3D) to two dimensional (2D) surfaces. If the energy of the interaction between the filaments and the substrate was in the range of the thermal energy, the filaments would be able to freely equilibrate on the substrate prior to adsorption, and the elastic properties would be conserved during the adsorption process. In this case, the value of the persistence length obtained in 2D is identical to the persistence length of the same filament in 3D (Mücke *et al.* 2004).

However, if the energy of the interaction between the filaments and the substrate is bigger than the thermal energy, the filaments would be kinetically trapped by the support before having equilibrated. In this case, the persistence length of the filaments in 2D will yield a smaller apparent persistence length, which depends on the surface adsorption mechanism (Mücke *et al.* 2004).

As displayed in **Table 4-1**, in all the environments that have been investigated, the persistence lengths (P_R) obtained by applying **Equation 4-2** were less than 5% of the persistence lengths (P_θ) obtained by applying **Equation 4-1**. One way to explain this could be, the kinetics of trapping, which likely initiates through the pinning of a few arbitrary points of the filament to the substrate and proceeds by the adsorption of the intermediate parts of the molecule. This suggests that the use of a global property such as end-to-end distance R to deduce persistence length may lead to an underestimation of the value of persistence length (Abels *et al.* 2006). However, assuming during kinetic trapping the angular distribution of the filament in 3D is preserved and the mechanical information is transferred onto the 2D plane, using local properties such as angle θ may obtain a more accurate value of persistence length.

The values of persistence length obtained above agreed with the persistence length obtained by Trachtenberg and Hammel (1992), which was from 4.5 to 41.14 μm . Using the persistence length obtained on gold in air ($13 \pm 3 \mu\text{m}$), the Young's modulus of *Salmonella* flagellar filaments could be estimated (**Equation 4-3**), which was $E = 22 \pm 4 \text{ MPa}$.

4.3 Change of Flexibility during Fibrillization of Lysozyme Fibrils

The fibrillization process of lysozyme fibrils was visualised using AFM (see section 3.2). Under certain conditions, lysozyme proteins were found to self-assemble from single proteins to protofilaments, and then the protofilaments intertwine with each other to form mature fibrils. An “n+1” model has been proposed to complete Khurana’s model (2003) to explain the hierarchical assembly levels of lysozyme (see section 3.2 for a detailed explanation of the fibrillization pathway).

Table 4-2 Persistence length of lysozyme protofilaments and fibrils of different assembly levels during fibrillization.

Models	Protofilaments	Fibrils				
		1+1	2+1	2+2	4+1	4+4
Persistence length P_0 (μm)	0.42 ± 0.07	16 ± 2	25 ± 3	28 ± 3	29 ± 3	52 ± 4
Young’s modulus E (GPa)	1.3 ± 0.6	8.9 ± 1.0	4.1 ± 0.8	3.1 ± 0.9	1.5 ± 0.3	1.0 ± 0.1

The fibril models are explained in detail in section 3.2. For example, lysozyme proteins self-assemble to protofilaments; two protofilaments intertwine with each other to form a “1+1” fibril; two “1+1” fibrils intertwine with each other to form a “2+2” fibril; a “1+1” fibril intertwine with a protofilament to form a “2+1” fibril; etc. The Young’s modulus E was obtained by bringing P_0 into **Equation 4-3**.

In order to obtain elasticity information during the fibrillization process for lysozyme fibrils, the persistence lengths were computed from the same AFM

topography images obtained to monitor structural changes during fibrillization (e.g. **Figure 3-16** and **Figure 3-18**; see section 3.2). Lysozyme protofilaments or fibrils were categorised by their heights, then through the application of **Equation 4-1**, their persistence lengths were obtained (see section 4.1). All calculated persistence lengths are displayed in **Table 4-2**.

The persistence length of a “1+1” fibril, which is the fibril composed of two protofilaments intertwining with each other, was found to be $16 \pm 2 \mu\text{m}$ (**Table 4-2**), which was 38 times of the persistence length of the protofilaments ($0.42 \pm 0.07 \mu\text{m}$) (**Table 4-2**). However, the persistence lengths of fibrils of different assembly levels were all found to be of the same order of magnitude. The persistence length of the “4+4” fibrils, which is that of the highest assembly level observed, was found to be $52 \pm 4 \mu\text{m}$, only 3 times the persistence length of the “1+1” fibrils. By bringing the persistence lengths into **Equation 4-3**, the Young’s moduli E were calculated (**Table 4-2**). Although the persistence length increased with the increasing of the assembly level, the Young’s modulus only increased from the protofilaments to “1+1” fibril, and then the Young’s modulus actually decreased with the increasing of the assembly level from “1+1” fibril to “4+4” fibril. In other words, the higher the assembly level of the fibrils, the less flexible the lysozyme fibrils appear to be, but the softer the fibrils are.

Gere stated in his book “Mechanics of Materials” (2004) about the elasticity of cables, which are constructed from wires wound together. “Under the same tensile load, the elongation of a cable is greater than the elongation of a solid bar of the same material and same metallic cross-sectional area, because the wires in a cable “tighten up” in the same manner as the fibers in a rope. Thus, the modulus of

elasticity (Young's modulus) of a cable is less than the modulus of the material of which it is made."

Assuming a lysozyme fibril is constructed from fibrils of a lower assembly level intertwined together, in the similar manner as a cable constructed from wires, the Young's modulus of this fibril could be less than the Young's modulus of the fibrils of the lower assembly level from which this fibril constructed. For instance, the "2+2" fibril is constructed from two "1+1" fibrils, and the Young's modulus of "2+2" fibril is 3.1 ± 0.9 GPa (Table 4-2), which is lower than the Young's modulus of "1+1" fibril (8.9 ± 1.0 GPa). The "4+4" fibril is constructed from two "2+2" fibrils, and the Young's modulus of "4+4" fibril is 1.0 ± 0.1 GPa, which is even lower than the Young's modulus of "2+2" fibril (3.1 ± 0.9 GPa). However, the Young's modulus of a protofilament is 1.3 ± 0.6 GPa, which is only ~15% of the Young's modulus of "1+1" fibril (8.9 ± 1.0 GPa). The intertwining of protofilaments to form a "1+1" fibril, seemed however to increase the Young's modulus. A reason could be that protofilaments do not simply intertwine with each other to form "1+1" fibrils; instead, protofilaments might undergo some structural change, in order to form "1+1" fibrils; which results the increasing of Young's modulus from protofilaments to "1+1" fibrils.

The average Young's modulus of protofilaments and fibrils of different assembly levels was found to be 3.3 GPa, which is consistent with that reported for insulin fibrils 3.3 GPa (Smith *et al.* 2006). Smith and co-workers obtained this 3.3 GPa value as an average value of insulin fibrils without specifying their assembly level.

4.4 Flexibility of diphenylalanine Fibrils

The diphenylalanine fibrils (FF fibrils) were found to range from several micrometers to over 100 μm in length (Reches and Gazit's 2003; Song *et al.* 2004). AFM images of FF fibrils on mica surface were obtained using a Nanoscope multimode AFM equipped with a J-scanner (Veeco, Santa Barbara, CA, USA), which has a maximum X-Y scan size $120 \times 120 \mu\text{m}^2$ (data sheet is available to download on manufacturer's website <http://veeco.com/>). However, with large X-Y scan sizes, or X-Y scan size close to the maximum, drift artefacts become common on AFM images (West and Starostina n.d.). A typical AFM image of FF fibrils taken during my experiments had X-Y scan size $10 \times 10 \mu\text{m}^2$ to $50 \times 50 \mu\text{m}^2$, and therefore most of the FF fibrils observed under AFM imaging exceeded the X-Y scan size. In other words, an AFM image could only capture fragment of a FF fibril, or fragments of FF fibrils. The obtained AFM images, most fragments of FF fibrils appeared to be “straight” and have infinite persistence length. Only a few fibrils with thinner diameter (40 to 50 nm in height) were captured with their whole length on one AFM image. Those fibrils were used to compute the persistence length and the Young's modulus.

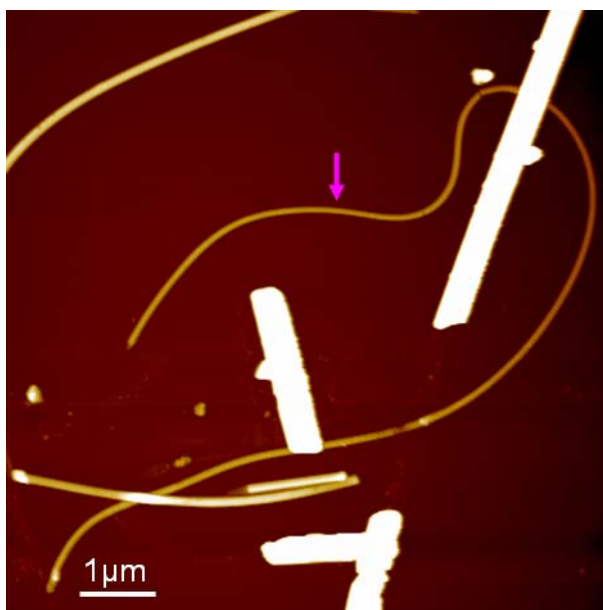


Figure 4-9 AFM image of FF nanotubes. The nanotubes indicated by a pink arrow is 40 ± 1 nm in height and has a persistence length P_0 22 ± 2 μm . The Z-range is 441.4 nm.

A FF fibril with thinner diameter is shown in **Figure 4-9** (indicated by a pink arrow). The height of this fibril is 40 ± 1 nm. The persistence length P_0 is 22 ± 2 μm . Using this persistence length, the Young's modulus of this fibril was computed 0.8 ± 0.2 MPa. This value is much smaller than the value of the Young's modulus obtained by Kol and co-workers (2005), which was ~ 19 GPa. Kol and co-workers studied FF fibrils with diameters ranging from 150 to 300 nm, and noted that the diameter of FF fibrils had no apparent effect on the elasticity of FF fibrils. One possible reason could be the effect of the diameter of FF fibrils on their elasticity falls off with the increasing of the diameter. In other words, within a lower diameter range (e.g. 40 to 150 nm), the elasticity of FF fibrils increases rapidly from MPa to GPa; within higher diameter range (e.g. 150 nm to 300 nm), the effect of the diameter on the elasticity of FF fibrils is within the experimental error. Unfortunately, as explained above, the persistence length method as a

means to calculate elasticity is not suitable for FF fibrils with bigger diameters. Therefore, a full assessment of the relation between the elasticity and the diameter of FF fibrils could not be achieved with the persistence length method (see section 6.3.1 for comparison).

4.5 Conclusion

Persistence length is a measure of the flexibility of a filamentous structure. If the geometry of the cross section of the filament is known, its Young's modulus of this filament can be obtained. AFM topography images of such structures show the contour of the filaments transformed from three dimensional to two dimensional surfaces. By analysing AFM images, the persistence lengths of filaments can be obtained.

In this chapter, the work of achieving the Young's moduli of *Salmonella* flagellar filaments, lysozyme fibrils and FF fibrils through measurement of persistence length has been presented. On gold surfaces and imaged in air, *Salmonella* flagellar filaments were found to have a persistence length of 13 μm , lysozyme fibrils of different assembly levels had a persistence lengths from 16 to 52 μm , and thin FF fibrils had a persistence length of 22 μm . Accordingly, *Salmonella* flagellar filaments have a Young's modulus 22 MPa, lysozyme fibrils an average Young's modulus 3.3 GPa, and thin FF fibrils a Young's modulus 0.8 MPa.

As limited by the range of scan size and the resolution of AFM imaging, the persistence length method presented here is not suitable for nanotubes or fibrils with too high or too low persistence length. The major errors of the persistence length methods include: the underestimation of the persistence length caused by

the transformation of nanotubes or fibrils from 3D to a 2D plane; the inaccuracy in determination of the diameter of the cross section of nanotubes or fibrils for calculation of the Young's modulus.

Chapter 5 Using the Adhesive Interaction between AFM Tips and Sample Surfaces to Measure the Elasticity of Protein Nanotubes

The adhesive interaction between the AFM tips and the sample surfaces can be used to provide the elastic information about the sample (Sun *et al.* 2004). Unlike indentation methods (Kol *et al.* 2005), this technique does not require location of the tip onto the centre of a protein nanotube and also minimises interference from the substrate (Akhremitchev and Walker 1999). In this chapter, the effect of the ionic strength on the elasticity of *Salmonella* flagellar filaments was investigated using the adhesive interaction method.

5.1 Theory and Method

5.1.1 The JKR (Johnson, Kendall and Roberts) Model

When an AFM tip approaches a soft sample, the adhesive force can draw the tip into the sample; when the AFM tip retracts from the soft sample, the tip can also pull the sample up because of the adhesive force (Sun *et al.* 2004). Considering the AFM tip as a sphere and using a spring to represent the AFM cantilever, the adhesive interaction between the AFM tip and a soft sample is shown in **Figure 5-1 (a)**. A typical force-versus-indentation curve is also shown in **Figure 5-1 (b)**.

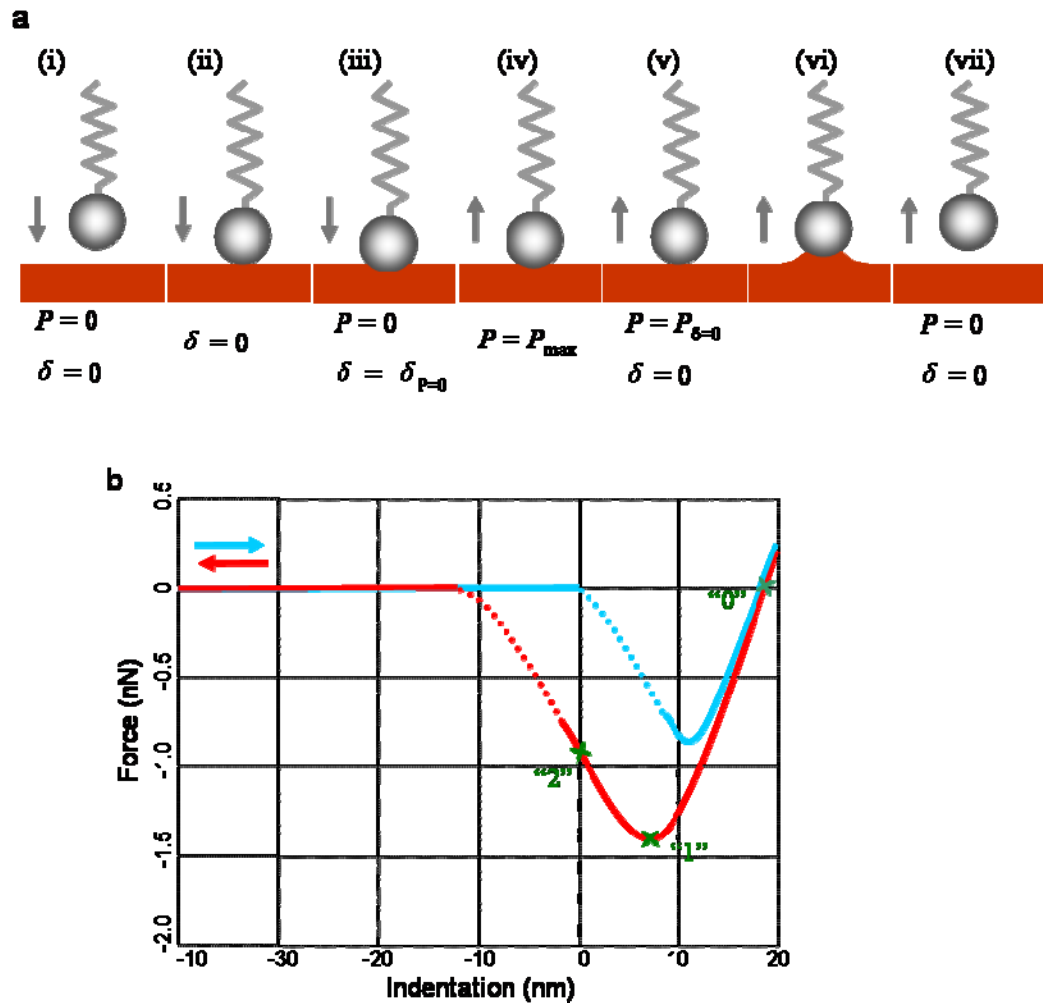


Figure 5-1 The adhesive interaction between the AFM tip and the sample. In (a), the AFM tip is represented as a sphere and the spring represents the AFM cantilever. The sequence shows: the AFM tip approaches (i) and contacts (ii) the sample; then the tip is drawn into the sample by the adhesive interaction (iii); when the tip retracts from the sample (iv, v), the sample will be pulled up by the adhesive force (vi) before it finally ruptures from the sample (vii). A typical force-versus-indentation curve is shown in (b). The blue curve is the approaching curve and the red curve is the retracting curve. On the retracting curve, point “0”, “1” and “2” are the moments represented on (iii), (iv) and (v), respectively (Sun *et al.* 2004).

The details of how to obtain a force-versus-indentation curve and how to define the zero indentation point is explained in section 2.1.1.3. Upon approach, the tip

jumps into contact with the sample surface at the point of mechanical instability, when the gradient of the interaction force exceeds the force constant of the cantilever. Once the tip contacts the surface, the tip is pulled into the sample by the adhesive interaction. At point “0” (**Figure 5-1** (a, iii) and (b)), there is zero external force on the AFM cantilever; the indentation of the sample is purely due to the adhesive interaction; and the stored elastic energy and the surface energy are balanced. At point “1” (**Figure 5-1** (a, iv) and (b)), the tip has a maximum external force. At point “2” (**Figure 5-1** (a, v) and (b)), the indentation is zero. Upon retraction of the tip from the sample, the tip pulls up the sample, and eventually becomes detached from the sample surface.

If the AFM tip and the sample are both treated as spheres and the radius a of the contact area is small (much smaller than both of the sphere radii), a theory proposed by Johnson, Kendall and Roberts (JKR theory) (1971) can be applied. The relationship between the external load P and the contact radius a , and the relationship between the indentation δ of the sample and the contact radius a are given by **Equation 5-1** and **Equation 5-2**, respectively.

$$a^3 = \frac{R}{K} \left\{ P + 3\pi R\gamma_{12} + \left[6\pi RP\gamma_{12} + (3\pi R\gamma_{12})^2 \right]^{\frac{1}{2}} \right\}$$

Equation 5-1

$$\delta = \frac{a^2}{R} \left[1 - \frac{2}{3} \left(\frac{a_{P=0}}{a} \right)^{\frac{3}{2}} \right]$$

Equation 5-2

where γ_{12} is the interfacial energy, $a_{P=0}$ is the contact radius under zero external load, K is a constant related to the elastic constants of the AFM tip and the sample, and R is the normalised radius of the two spheres. K and R are given by **Equation 5-3** and **Equation 5-4**, respectively.

$$K = \frac{4}{3\pi(k_{\text{tip}} + k_{\text{sample}})}$$

Equation 5-3

$$R = \frac{R_{\text{tip}} R_{\text{sample}}}{R_{\text{tip}} + R_{\text{sample}}}$$

Equation 5-4

where k_{tip} and k_{sample} are the elastic constants of the AFM tip and the sample respectively, and R_{tip} and R_{sample} are the tip radius and the sample radius, respectively. k_{tip} and k_{sample} are related to the elastic modulus of the tip and the sample as given by **Equation 5-5** and **Equation 5-6**, respectively.

$$k_{\text{tip}} = \frac{1 - \nu_{\text{tip}}^2}{\pi E_{\text{tip}}}$$

Equation 5-5

$$k_{\text{sample}} = \frac{1 - \nu_{\text{sample}}^2}{\pi E_{\text{sample}}}$$

Equation 5-6

where ν is the Poisson ratio and E_{tip} and E_{sample} is the Young's modulus of the tip and sample, respectively. Because the sample radius is much larger than the tip radius, the normalised radius is equivalent to the tip radius: $R = R_{\text{tip}}$ ($R_{\text{tip}} \ll R_{\text{sample}}$).

The generally used AFM silicon nitride tip has a Young's modulus ~220 GPa while the Young's modulus of the silicon cantilever ~190 GPa (Cuenot *et al.* 2000). The protein nanotube of interest has a Young's modulus only ~20 MPa (Trachtenberg and Hammel 1992 and also see section 4.2.4). Therefore, combining **Equation 5-3**, **Equation 5-5** and **Equation 5-6**:

$$E_{\text{sample}} = \frac{3(1-\nu_{\text{sample}}^2)}{4} K \quad (E_{\text{tip}} \gg E_{\text{sample}})$$

Equation 5-7

For each point on the force-versus-indentation curve, there are three variables: the contact radius a , interfacial energy γ , and Young's modulus of the sample E_{sample} . The external load P and the indentation δ can be read directly from the force-versus-indentation curve. Combining any two points on the force-versus-indentation curve, using **Equation 5-1** and **Equation 5-2**, a , γ and E_{sample} can be obtained (Sun *et al.* 2004). For the ease of data processing, special points on the force-versus-indentation curve are chosen: the point where $P = 0$ (**Figure 5-1 b**, point "0") and the point where $\delta = 0$ (**Figure 5-1 b**, point "2").

At the point $P = 0$, **Equation 5-1** and **Equation 5-2** become:

$$a_{P=0}^3 = \frac{6\pi R^2 \gamma_{12}}{K}$$

Equation 5-8

$$\delta_{P=0} = \frac{a_{P=0}^2}{3R}$$

Equation 5-9

At point $\delta = 0$, **Equation 5-1** and **Equation 5-2** become:

$$a_{\delta=0}^3 = \frac{R}{K} \left\{ P_{\delta=0} + 3\pi R\gamma_{12} + \left[6\pi R P_{\delta=0} \gamma_{12} + (3\pi R\gamma_{12})^2 \right]^{\frac{1}{2}} \right\}$$

Equation 5-10

$$\left(\frac{a_{P=0}}{a_{\delta=0}} \right)^{\frac{3}{2}} = \frac{3}{2}$$

Equation 5-11

Combining **Equation 5-8** and **Equation 5-10**, then **Equation 5-11**:

$$P_{\delta=0} = -\frac{4}{3} \pi R \gamma_{12}$$

Equation 5-12

where the negative sign means the external load is on the direction of retraction from the sample.

Combining **Equation 5-8**, **Equation 5-9** and **Equation 5-12**:

$$K = \frac{-P_{\delta=0}}{2} \left(\frac{3}{R\delta_{P=0}^3} \right)^{\frac{1}{2}}$$

Equation 5-13

Bringing **Equation 5-13** into **Equation 5-7**:

$$E_{\text{sample}} = \frac{3(\nu_{\text{sample}}^2 - 1)P_{\delta=0}}{8} \left(\frac{3}{R\delta_{P=0}^3} \right)^{\frac{1}{2}}$$

Equation 5-14

From **Equation 5-14**, the Young's modulus of the sample can be obtained.

5.1.2 Applying JKR Model to Obtain the Young's Modulus of a Sample

In this section, the details of data processing of a typical force-versus-indentation curve will be explained with an example.

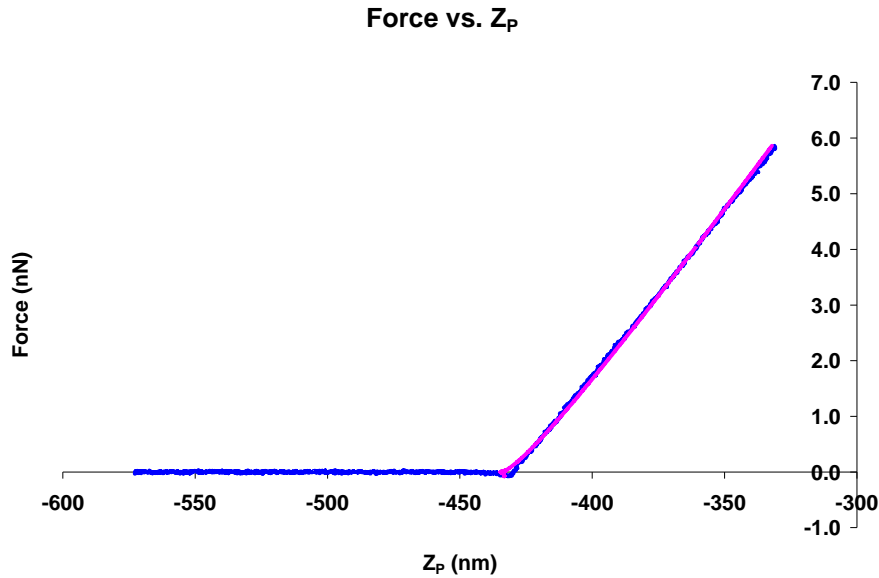
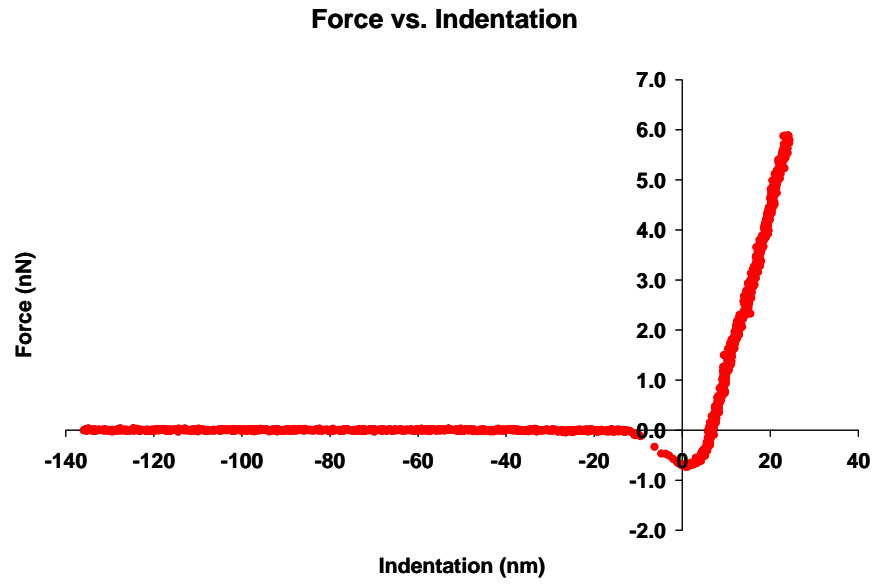


Figure 5-2 A force-versus-displacement approach curve. A silicon nitride tip was used, with the spring constant k_c of 0.07292 N/m determined by thermal method (see section 2.1.1.3). *Salmonella* flagellar filaments were deposited onto mica surface (see section 2.2). The experiment was carried out in PBS buffer with MgCl_2 ($I = 0.1$ M, $c_{\text{PBS}} = 0.01$ M, $c_{\text{Mg}^{2+}} = 0.01$ M, pH 7.0). The blue curve is the experimental data curve. The pink curve is the fitting curve with Hertzian model (see section 2.1.1.3). $Z_{p0} = -434.7 \pm 0.1$ nm were obtained by the fitting.

The force-versus-displacement approach curve of a silicon nitride tip ($k_c = 0.07292$ N/m) on *Salmonella* flagellar filaments in buffer solution is shown on **Figure 5-2**. In order to find the zero piezo displacement point, the experimental data in the range when the tip and sample came into contact were fitted with a Hertzian model (see section 2.1.1.3).

a



b

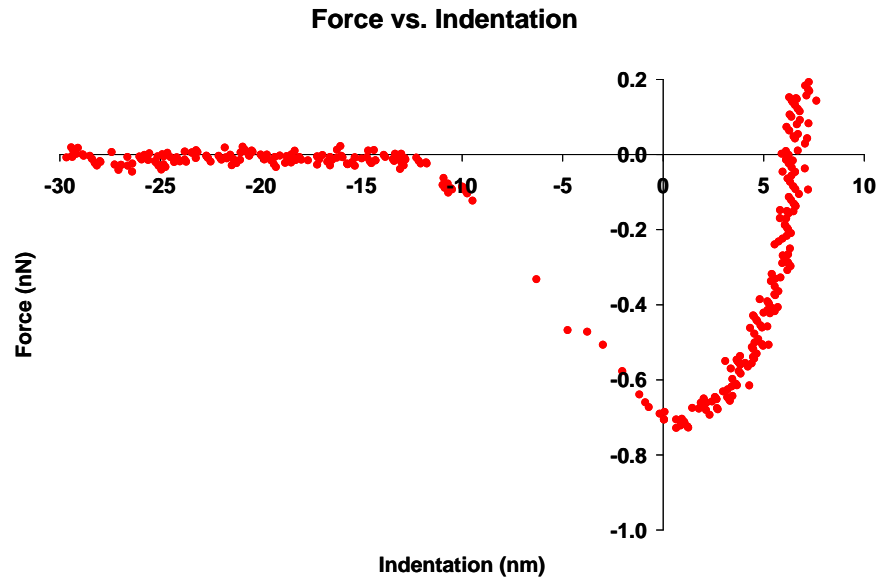


Figure 5-3 The force-versus-indentation retract curve from the same experiment of **Figure 5-2**. (a) is the whole retract curve and (b) is zoomed part of the curve. Reading from (b), there are $P_{\delta=0} = 0.69$ nN and $\delta_{P=0} = 6.7$ nm.

Using the zero piezo displacement obtained from fitting to the approach curve, the force-versus-indentation retract curve could be obtained (**Figure 5-3**). The values $P_{\delta=0} = 0.69$ nN and $\delta_{P=0} = 6.7$ nm were read directly from the force-versus-indentation retracting curve. Tip radius $R = 3.0$ nm was obtained using blind reconstruction method with SPIP software (see section 2.1.3). Blind reconstruction is a technique of estimating the geometry of AFM tip from the topographic image data (Villarrubia 1997; Williams *et al.* 1996). A thin film of porous aluminum consisting of hexagonal hollow cells (Mikromash, USA) was imaged using the same tip used in the adhesive interaction experiment in order to estimate the geometry of the tip. Bringing all these values to **Equation 5-14** resulted $E = 11.2$ MPa.

A number of force curves under the same conditions were then obtained in order to calculate the average Young's modulus (**Figure 5-4**). The average Young's modulus E of *Salmonella* flagellar filaments under this condition was $E = 7.2 \pm 0.8$ MPa.

A control experiment has also been done under the same condition. A retract force curve obtained on mica surface in buffer solution is displayed in **Figure 5-5**. The mica surface is hard with a high Young's modulus (140 to 200 GPa, manufacturer's data), and it can be treated as a non-deformable surface with attraction force (see section 2.1.1.3).

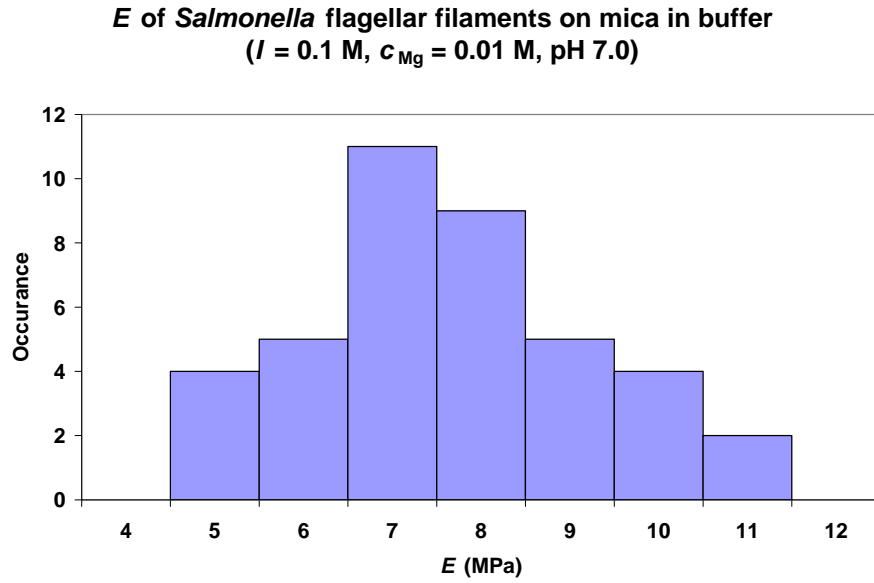


Figure 5-4 Histogram of Young's modulus E of *Salmonella* flagellar filaments on mica in PBS buffer with MgCl_2 ($I = 0.1$ M, $c_{\text{PBS}} = 0.01$ M, $c_{\text{Mg}^{2+}} = 0.01$ M, pH 7.0) obtained using adhesive interaction method. The mean Young's modulus $E = 7.2 \pm 0.8$ MPa ($N = 40$).

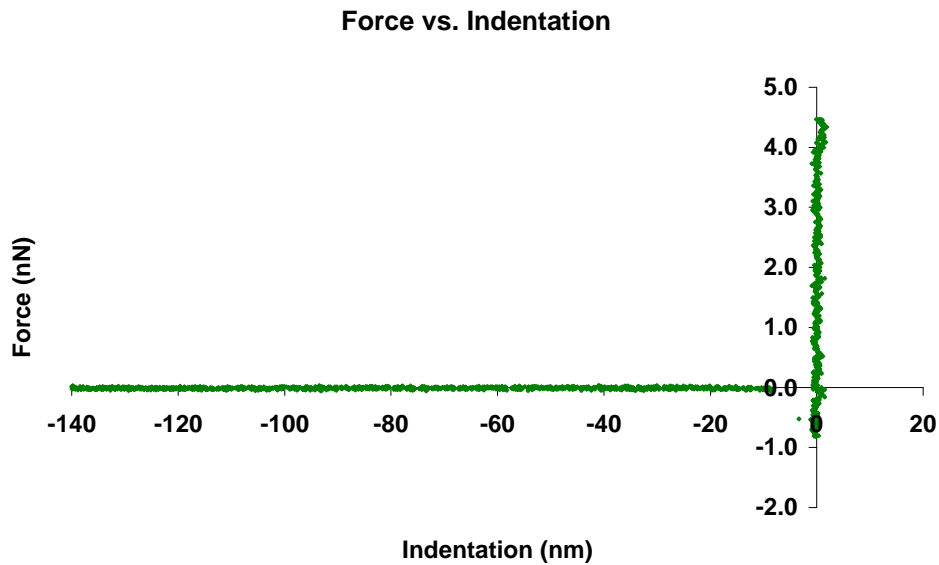


Figure 5-5 The force-versus-indentation retractor curve from the control experiment. The force curve was obtained on mica surface in PBS buffer with MgCl_2 ($I = 0.1$ M, $c_{\text{PBS}} = 0.01$ M, $c_{\text{Mg}^{2+}} = 0.01$ M, pH 7.0). The same tip was used as in the experiment of **Figure 5-2** and **Figure 5-3**.

5.2 The Effects of the Ionic Strength on the Elasticity of *Salmonella* Flagellar Filaments

In a similar manner as explained in the previous section, force curves of *Salmonella* flagellar filaments on mica in different buffer solutions were obtained and the Young's modulus calculated using the JKR model (Johnson, Kendall and Roberts 1971).

Keeping the ionic strength I constant ($I = 0.5$ M, $c_{\text{PBS}} = 0.01$ M, pH 7.0), while changing the concentration of Mg^{2+} , the Young's modulus E of *Salmonella* flagellar filaments was obtained (Table 5-1).

Table 5-1 Young's modulus E of *Salmonella* flagellar filaments in buffer solutions with different concentrations of Mg^{2+} .

Ionic strength I (M)	Concentration of Mg^{2+} $c_{\text{Mg}^{2+}}$ (M)	Young's modulus E (MPa)
0.5	0.01	13.0 ± 1.8
0.5	0.05	12.0 ± 2.6
0.5	0.1	13.5 ± 2.2

Salmonella flagellar filaments were deposited on mica surfaces in buffer solutions ($c_{\text{PBS}} = 0.01$ M, pH 7.0, pH adjusted using HCl or NaOH, I adjusted using NaCl). The Young's modulus E was obtained using adhesive interaction method explained in previous section.

There was no statistically significant difference among the three Young's modulus groups with $c_{\text{Mg}^{2+}}$ of 0.01M, 0.05M and 0.1M. Therefore there was no obvious relation between E and $c_{\text{Mg}^{2+}}$ (Table 5-1). However, when the concentration of Mg^{2+} was kept constant, the Young's modulus of *Salmonella*

flagellar filaments increased with the increasing of ionic strength of the solutions (Table 5-2).

Table 5-2 Young's modulus E of *Salmonella* flagellar filaments in buffer solutions with different ionic strength.

Ionic strength I (M)	Concentration of Mg^{2+} $c_{Mg^{2+}}$ (M)	Young's modulus E (MPa)
0.1	0.01	7.2 ± 0.8
0.5	0.01	13.0 ± 1.8
1.0	0.01	18.6 ± 4.5

Salmonella flagellar filaments were deposited on mica surface in buffer solutions ($c_{PBS} = 0.01$ M, pH 7.0, pH adjusted using HCl or NaOH, I adjusted using NaCl). The Young's modulus E was obtained using adhesive interaction method explained in previous section.

Table 5-3 Summary of Young's modulus E of *Salmonella* flagellar filaments in different buffer solutions.

Ionic strength I (M)	Concentration of Mg^{2+} $c_{Mg^{2+}}$ (M)	Young's modulus E (MPa)
0.1	0.01	7.2 ± 0.8
0.5	0.01	13.0 ± 1.8
0.5	0.05	12.0 ± 2.6
0.5	0.1	13.5 ± 2.2
1.0	0.01	18.6 ± 4.5
1.0	0.2	20.5 ± 5.3

Salmonella flagellar filaments were deposited on mica surface in buffer solutions ($c_{PBS} = 0.01$ M, pH 7.0, pH adjusted using HCl or NaOH, I adjusted using NaCl). The Young's modulus E was obtained using adhesive interaction method explained in previous section.

All the experimental results of Young's modulus E of *Salmonella* flagellar filaments obtained using adhesive interaction method were summed up and displayed in Table 5-3. Young's modulus E was plotted against the ionic strength I of the buffer solutions (Figure 5-6).

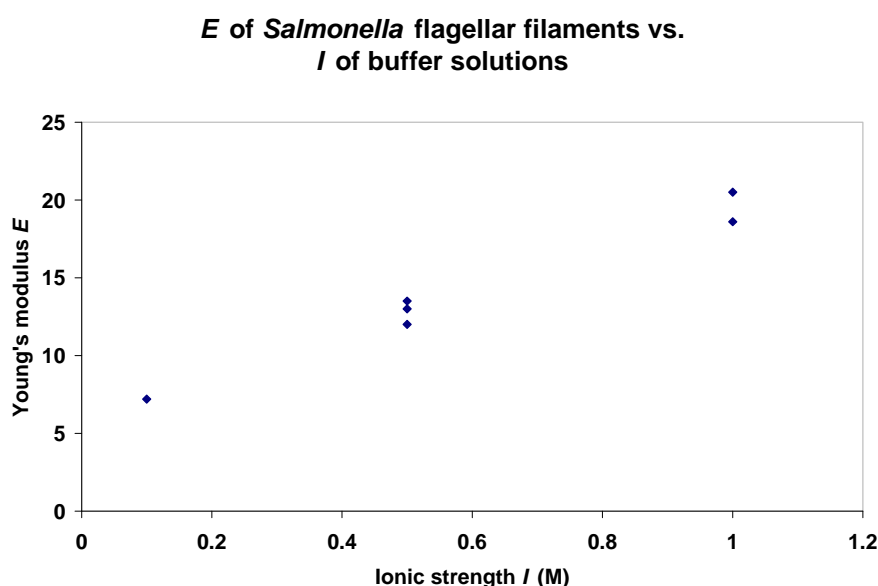


Figure 5-6 Young's modulus E of *Salmonella* flagellar filaments versus the ionic strength I of buffer solutions. *Salmonella* flagellar filaments were on mica surface in buffer solutions ($c_{\text{PBS}} = 0.01$ M, pH 7.0, pH was adjusted using HCl or NaOH, I was adjusted using NaCl). Data is from Table 5-3. The error bars are not shown for clarity.

As explained in section 3.1, Mg^{2+} acts as a bridge between *Salmonella* flagellar filaments and the mica surface in pH 7.0 buffer solution to immobilise the filaments onto the substrate. Using the adhesive interaction method, the concentration of Mg^{2+} (from 0.01M to 0.2M) in buffer solutions was found not to have an effect on the elasticity of *Salmonella* flagellar filaments. However, when the ionic strength of the buffer solutions (regulated by NaCl) increased, the

Young's modulus of *Salmonella* flagellar filaments increased. In other words, the higher the ionic strength of the buffer is, the harder *Salmonella* flagellar filaments appeared to become (Adami *et al.* 1999; Srigiriraju *et al.* 2005). This discovery showed the potential of flagellar filaments as smart materials. The alteration of elasticity of flagellar filaments can be easily controlled by modifying the ionic strength of the fluidic environment they are in.

One systematic error of the resulting Young's modulus from this adhesive interaction method is caused by the determination of the tip radius R . As explained in section 5.1.2, the tip radius R was obtained by using the blind reconstruction method provided by SPIP software (Villarrubia 1997; Williams *et al.* 1996). However, only the radius of the “worst case tip” can be obtained by this method. This “worst case tip” is the tip that is able to scan all parts of the surface with its apex, but the tip might be sharper in reality. This brought a possible error on the Young's modulus obtained using **Equation 5-14**. If the tip in reality is 10% sharper, the value of the Young's modulus would be 5% greater than calculated.

In order to apply the adhesive interaction method to *Salmonella* flagellar filaments in buffer solutions without Mg^{2+} , the force-versus-indentation curves in these solutions were obtained. However, the force-versus-indentation curves in buffer solutions without Mg^{2+} did not show an adhesive part, instead, they had plateaux.

5.3 Investigating the Interaction between *Salmonella* Flagellar Filaments and Mica Substrates in Electrolyte Environments

As presented in section 3.1, the AFM tapping mode images of *Salmonella* flagellar filaments on mica in pH 7.0 buffer solution containing Mg^{2+} were obtained. If Mg^{2+} was not present, the *Salmonella* flagellar filaments could not be immobilised onto the mica surface and allow scanning of AFM tip. However, the force curves of *Salmonella* flagellar filaments could be obtained within this environment. Unlike the force curves of *Salmonella* flagellar filaments on mica in pH 7.0 solution with Mg^{2+} , there were visible plateaux in those force curves. The force-versus-indentation curves collected had either one or two plateaux (e.g. the force curve in **Figure 5-7** has two plateaux). Force curve consisting more than two plateaux was not found during my experiments. A typical force-versus-indentation curve of *Salmonella* flagellar filaments on mica in pH 7.0 buffer without Mg^{2+} is shown in **Figure 5-7**.

There are two visible plateaux in the force-versus-indentation curve in **Figure 5-7**. The heights of the plateaux most likely reflect the constant equilibrium desorption forces resulting from the process of peeling off one or more individual filaments from the surface with the AFM tip (Friedsam *et al.* 2004). In this particular sample (**Figure 5-7**), the heights of the two plateaux are $F_1 = 0.11$ nN and $F_2 = 0.21$ nN. These two values are the average of the heights of all the experimental points of each plateau respectively. The more negative end (the end on the direction of retracting the tip from the surface) of each plateau could represent the rupture of the filament from the mica surface or from the AFM tip. The lengths of plateaux, which will be referred as desorption lengths in this

section, correspond to partial or full lengths of the desorbed filaments. In this particular sample (**Figure 5-7**), the lengths are $l_1 = 151$ nm, $l_2 = 183$ nm.

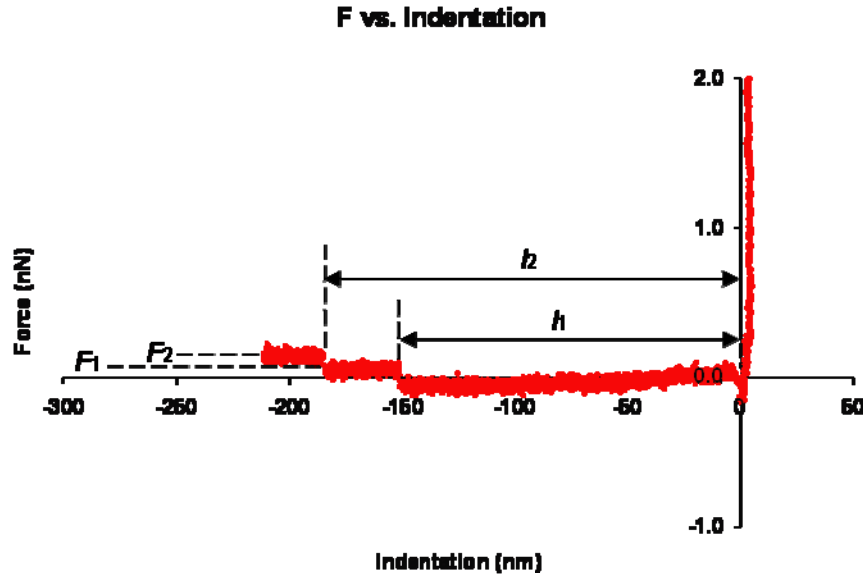


Figure 5-7 A force-versus-indentation retracting curve of *Salmonella* flagellar filaments on mica surface in pH 7.0 buffer ($c_{\text{PBS}} = 0.01$ M) without Mg^{2+} . A silicon nitride tip was used. There are two visible plateaux with heights $F_1 = 0.11$ nN and $F_2 = 0.21$ nN and length $l_1 = 151$ nm and $l_2 = 183$ nm.

In order to do batch analysis of the plateaux, I developed a programme “Stepfinder” written in Visual Basic for Application (VBA) language for Microsoft Excel. The stepfinder programme reads the X-Y coordinates of force-versus-indentation curves and calculates the central difference of the function $P = f(\delta)$ (where P is the force and δ is the indentation) (Abramowitz and Stegun 1972). The central difference is then plotted against the indentation δ . The peaks on the central difference curve correspond to the starting and ending points of the plateaux on the force-versus-indentation curve. Using the points between the

starting and ending points of the plateaux, the average of the forces and the lengths of the plateaux can be obtained. All the experimental points between the starting and ending points of a plateau were used to calculate the average desorption force and the desorption length. This programme considerably accelerated the speed of the data process. The following histogram of the desorption forces was obtained (Figure 5-8).

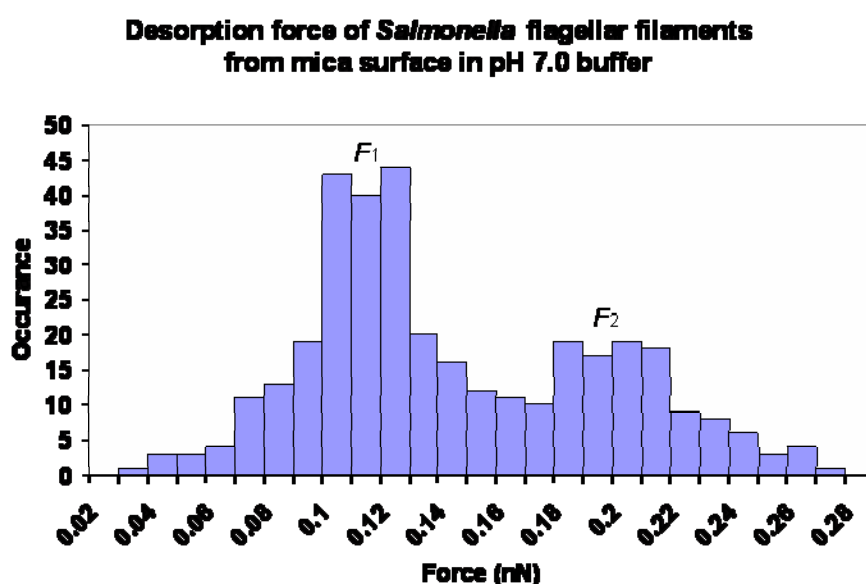


Figure 5-8 Histogram of desorption forces of *Salmonella* flagellar filaments from mica surface in pH 7.0 buffer without Mg^{2+} . Two peaks on this histogram are $F_1 = 0.11 \pm 0.1$ nN and $F_2 = 0.20 \pm 0.1$ nN (N = 344).

As shown in **Figure 5-8**, there are two peaks on the histogram of desorption forces (F_1 and F_2). By fitting Gaussian distributions to the two peaks separately, $F_1 = 0.11 \pm 0.1$ nN and $F_2 = 0.20 \pm 0.1$ nN were obtained. The peaks on the histogram of desorption force reflect the force required to peel off one or more flagellar filaments from the mica surface (Friedsam *et al.* 2004). The F_1 and F_2 on

the histogram correspond to the F_1 and F_2 plateaux on the force-versus-indentation curve (**Figure 5-7**). Considering F_2 is approximately two times of F_1 , if F_1 is the force required to peel off a single flagellar filament from the mica surface, F_2 could be the force required to peel off two flagellar filaments from the mica surface at the same time.

The desorption length of *Salmonella* flagellar filaments on mica surface in pH 7.0 buffer without Mg^{2+} was found to be from 4 nm to 197 nm. This value range is lower than the value range of the length of *Salmonella* flagellar filaments obtained by AFM imaging 1.0 to 3.0 μm (see section 3.1). One way to explain this difference could be that the desorption length of the filament is only part of a whole filament. In other words, the picking up and peeling off process by AFM tip were only applied to part of the filament. The reason why this happened is most likely that the AFM tip picked up a filament from the middle of the filament instead of from the end, or the rupture of the filament from the AFM tip could happen before the full length of filament had peeled off the surface.

This experiment showed that the adhesive interaction method requires the filaments to be immobilised onto the substrate surface. In pH 7.0 buffer, with Mg^{2+} , *Salmonella* flagellar filaments could be immobilised onto mica surface and the adhesive interaction method could be applied to obtain the elasticity (see previous section 5.2). However, without Mg^{2+} , in pH 7.0 buffer, *Salmonella* flagellar filaments would be picked up and peeled off the mica surface by AFM tip. This peeling off experiment could be utilised to access the desorption forces between the protein nanotubes and different substrate surfaces, which could provide the information of manipulating protein nanotubes individually.

5.4 Conclusion

If a protein nanotube is properly immobilised onto a substrate surface, when an AFM tip retracts from the surface of the soft protein nanotube, the tip can pull up and deform the sample because of the adhesive force. This deformation of the protein nanotube is related to its elasticity. In this chapter, the JKR (Johnson, Kendall and Roberts 1971) model has been applied to obtain the elastic information of *Salmonella* flagellar filaments, and the effect of the ionic strength on the elasticity of *Salmonella* flagellar filaments investigated.

The Young's modulus of *Salmonella* flagellar filaments was found to be from 7.2 MPa to 21.5 MPa. The concentration of Mg^{2+} (from 0.01 M to 0.2 M) in buffer solutions was found not to have effect on the elasticity of *Salmonella* flagellar filaments. However, when the ionic strength of the buffer solutions increased, the Young's modulus of *Salmonella* flagellar filaments increased.

The adhesive interaction method requires the protein nanotubes to be immobilised onto the substrate surface. Without Mg^{2+} , in pH 7.0 buffer, *Salmonella* flagellar filaments could be picked up and peeled off the mica surface by AFM tip with a desorption force of 0.11 nN.

Chapter 6 Using the Bending Beam Model to Estimate the Elasticity of Protein Nanotubes

If a protein nanotube can be placed over a cavity of the substrate, a suspended beam configuration is produced at the nanoscale. The beam will have different degrees of bending with different loading forces acting on it, related to its elastic properties. By using an AFM probe to apply loading forces on a protein nanotube, its elastic properties can therefore be obtained. In this chapter, the bending beam model is explained and then applied to protein nanotubes for this type of analysis.

6.1 Theory

6.1.1 Deformation of a Fixed-End Bending Beam

As explained in Gere's book "Mechanics of Materials" (1991) for the case of a concentrated load acting at the midpoint of a suspended fixed-end beam, using a unit-load method, the deflections at the midpoint of the beam when considering the effects of both bending moments and shear forces is as follows:

$$\begin{aligned}\delta &= \delta_B + \delta_S \\ &= FL^3 / 192EI + f_s FL / 4GA\end{aligned}$$

Equation 6-1

where δ is the deflection, δ_B is the deflection due to bending, δ_S is the deflection due to shearing; E is the Young's modulus, G is the shear modulus; F is the loading force; L is the suspended length; f_s is a cross-sectional property called the form factor for shear, which is a dimensionless quantity that can be evaluated for each particular shape of beam ($f_s = 10/9$ for a cylindrical beam); A is the cross-sectional area of the fibril; I is the moment of inertia of area A ($I = \pi D^4/64$ for a filled circular area with diameter D , $I = \pi(D_o^4 - D_i^4)/64$ for a tubular circular area with outer diameter D_o and inner diameter D_i).

We define E_{bending} as the bending modulus that corresponds to the Young modulus that would be deduced if shear deformations were neglected:

$$\begin{aligned}\delta &= \delta_B + \delta_S \\ &= FL^3 / 192EI + f_s FL / 4GA \\ &= FL^3 / 192E_{\text{bending}} I\end{aligned}$$

Equation 6-2

From **Equation 6-2**, there is:

$$1 / E_{\text{bending}} = 1 / E + (48f_s I / GA)(1 / L^2)$$

Equation 6-3

For a beam with several different suspended lengths, the Young's modulus can be obtained from the intercept of the plot of $1/E_{\text{bending}}$ versus $1/L^2$ and the shear modulus can be obtained from the gradient.

6.1.2 Applying the Bending Beam Model to Nanotubes

If a protein nanotube can be placed over a cavity of the substrate, a suspended beam configuration at the nanoscale is produced (**Figure 6-1**). Assuming the two ends are clamped, the elastic deformation in the middle of the suspended part of

the fibril resulting from a concentrated load can be expressed as **Equation 6-1** (Salvetat *et al.* 1999; Kis *et al.* 2002; Niu *et al.* 2007).

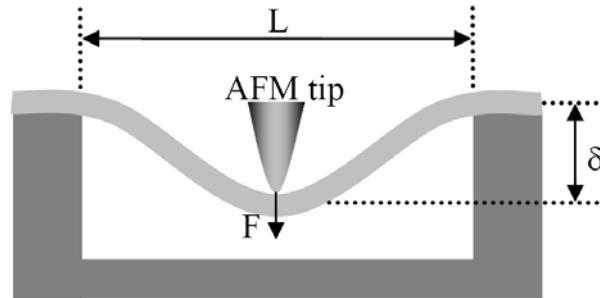


Figure 6-1 Schematic of the suspended beam configuration produced by a protein nanotube lying over a cavity on the substrate. The AFM is used to apply a loading force to the protein nanotube and to determine directly the resulting deflection (figure adapted from Niu *et al.* 2007).

The deflection δ , the suspended length L and the second moment I can be obtained from the profiles of the AFM images of the protein nanotubes. F is the AFM loading force on the nanotube, which is considered as a concentrated force midway along the suspended length of the nanotube. In contact mode AFM images, the loading force is equal to the product of the cantilever deflection, the deflection sensitivity and the spring constant of the AFM probe (see section 2.1.1.3 for the details of calculating force). From **Equation 6-2**, E_{bending} can be calculated. Because E_{bending} depends on the dimension of the protein nanotube from which it is calculated (**Equation 6-2**), in order to compare the elasticity under different experimental conditions by the means of comparing E_{bending} , the same nanotube was used.

In order to obtain Young's modulus E and shear modulus G from **Equation 6-3**, a protein nanotube lying across several holes of the substrate with different suspended length L was found. Assuming the geometry of the cross section remains the same along the protein nanotube, the Young's modulus can be obtained from the intercept of the plot of $1/E_{\text{bending}}$ versus $1/L^2$, and the shear modulus from the gradient.

6.2 β 2-microglobulin Fibrils Lying over Gaps within the Gold

Substrate

An attempt to apply the bending beam model to β 2-microglobulin fibrils was made. The β 2-microglobulin protein solution was incubated at 37°C for 5 days (see section 2.2.3 for the details of sample preparation). The resulting fibrils (**Figure 6-2**) were found to have an average height of 5.8 ± 0.8 nm and lengths from ~ 200 nm up to ~ 4 μ m ($N = 100$). Some fibrils with clear periodicity were observed (**Figure 6-2**) (detailed morphology studies of β 2-microglobulin fibrils by AFM can be found in Kad *et al.* 2003 and Gosal *et al.* 2005).

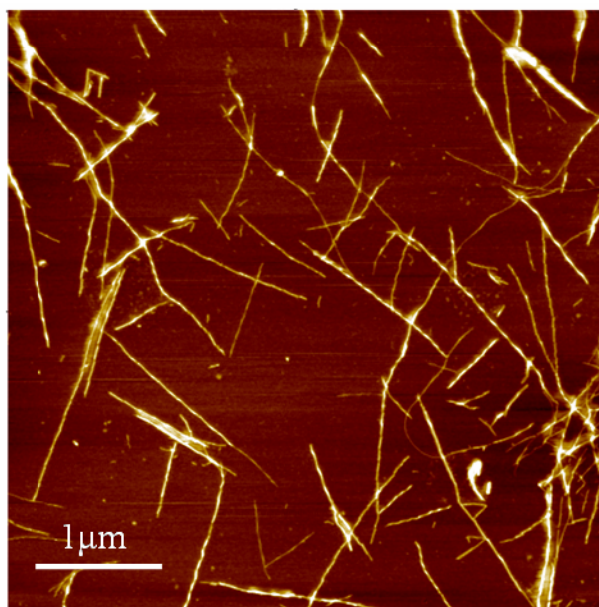


Figure 6-2 AFM height image of β 2-microglobulin fibrils after 5 days of incubation. The Z-range is 21.6 nm.

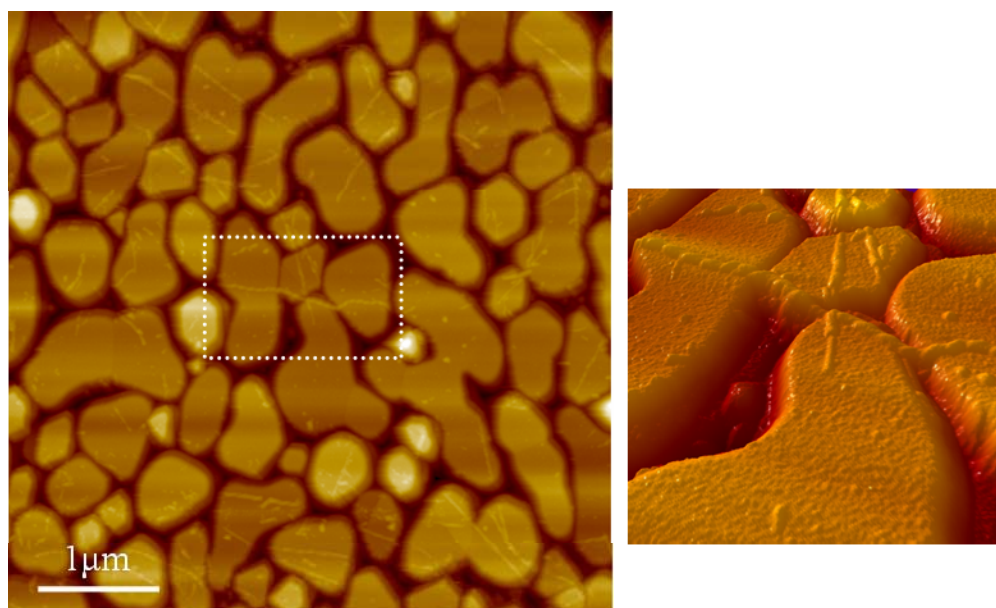


Figure 6-3 AFM image of β 2-microglobulin fibrils obtained in water on gold surfaces. The image on the left is a tapping mode height image. The picture on the right is a 3D representation (generated by SPIP software; see section 2.1.3) of the fibril in the centre of the left image indicated by the white dot-line rectangle.

The gold substrate obtained using evaporation gold coater (see section 2.2.5) has atomically flat islands (typically 0.2 μm to 1.0 μm in width), separated by gaps ~30 nm to ~150 nm in width. If a β 2-microglobulin fibril can be placed over a gap of gold substrate, a suspended beam configuration is produced. However, in order to obtain the value of the loading force (see section 6.1), AFM contact mode images of β 2-microglobulin fibrils needed to be obtained. Contact mode AFM imaging applies higher lateral forces on a sample than tapping mode (see section 2.1.1.2). A β 2-microglobulin fibril lying over a gap on a gold surface (**Figure 6-3**) was imaged in tapping mode. When switched to contact mode (in order to calculate the forces applied, for the bending beam model), the fibril broke over the gap. No contact mode images of β 2-microglobulin fibrils lying over gaps were obtained throughout these studies.

An attempt to apply the bending beam model to *Salmonella* flagellar filaments was also made and the similar situation as for β 2-microglobulin fibrils was found: both *Salmonella* filaments and lysozyme fibrils did not survive the imaging process i.e. they broke over the gaps of gold substrate, most likely due to the force applied by the AFM tip during contact mode imaging.

6.3 Elasticity of diphenylalanine Fibrils

The bending beam model was successfully applied to AFM images of diphenylalanine nanotubes (FF nanotubes) suspended across cavities. A micropatterned silicon substrate (with holes of 5 $\mu\text{m} \times 5 \mu\text{m}$ and 200 nm deep) (see section 2.2.5) was used to provide cavities for the suspended beam configuration (Gere 1991).

To prepare samples an aliquot of 10 μL of fresh FF nanotubes sample solution (see section 2.2 for the details of sample preparation) was dropped onto a UV cleaned micropatterned silicon substrate and subsequently dried under a gentle flow of nitrogen. This protocol produced fibrils which were found to occasionally lie over the holes of the substrate.

6.3.1 Elasticity of FF Nanotubes at Room Temperature

What is a “good” deflection?

From Equation 6-2, with the same loading force F and the suspended length L , the deflection δ increases with the decrease of the diameter D of the cross section of the fibril. The range of the loading force in AFM experiments can vary from nN to μN in an ambient atmosphere (Seo and Jhe 2008). The micropatterned silicon substrate employed had square shaped holes of $5\text{ }\mu\text{m} \times 5\text{ }\mu\text{m}$, which meant that the suspended length was up to $7\text{ }\mu\text{m}$ (the length of the diagonals of the holes). The deflection was up to the depth of the holes of the substrate, which was 200 nm. In practice, FF nanotubes with the cross section of around 150-200 nm in diameter were found to provide good bending beam configurations.

Examples of FF nanotubes lying over holes of the silicon grid with different deflections are displayed in Figure 6-4 (details of AFM analysis see section 2.1.2). The deflection of the fibril is the vertical difference between the middle of the suspended part and the part of the nanotube lying on the silicon substrate before or after the hole. The two points taken to measure the deflection theoretically also need to be on the centre of the cross section of the fibril (Figure 6-4 (i)) (Gere 1991).

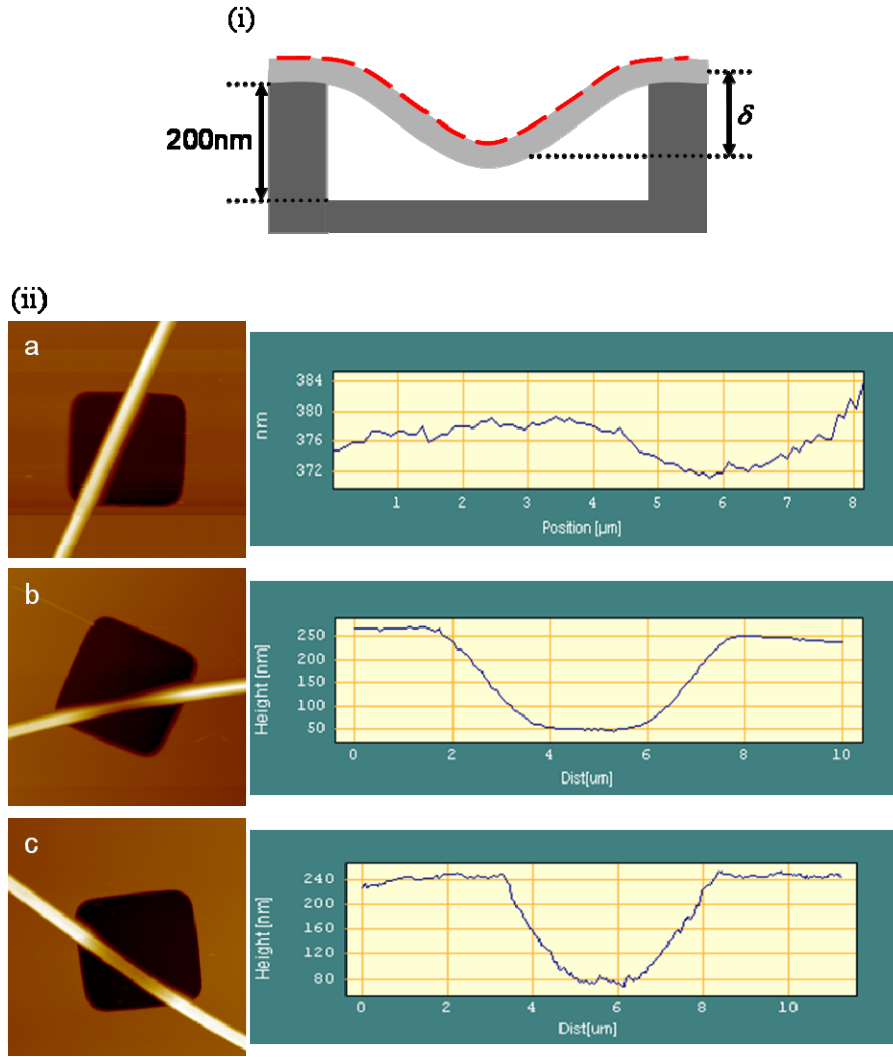


Figure 6-4 Examples of FF nanotubes lying over holes of the silicon substrate with different deflections. (i) A schematic showing a fibril lying over a hole. The depth of the hole is 200 nm. The red broken line indicates where the profiles in (ii) are. (ii) (a) A FF nanotube over a hole with negligible deflection. The profile on the right shows that the vertical difference along the fibril was ~10 nm. (b) A FF nanotube touching the bottom of the hole of the substrate. The profile on the right shows the deflection was ~200 nm. However, ~2 μm (from ~4 μm to ~6 μm on the x axis) of the fibril seems horizontal, which indicates that it is most likely touching the bottom of the hole. (c) A FF nanotube over a hole with a "good" deflection. The profile on the right shows the deflection was 160 nm. The size of each image in (ii) is 10 $\mu\text{m} \times 10 \mu\text{m}$. The Z-range of each image in (ii) is 1.035 μm , 1.137 μm and 966.5 nm, respectively.

However, the profiles obtained from AFM height images only show the heights of the upper surface of the sample. Therefore, assuming the geometry of the cross section remains the same along the fibril, the surface profiles on the top along the fibril (**Figure 6-4 (i)**, indicated by red dot-line) also represent the profiles along the centre of the fibril. A FF nanotube over a hole with negligible deflection, a FF nanotube touching the bottom of the hole of the substrate and a FF nanotube over a hole with a “good” deflection are shown in **Figure 6-4 (ii)**.

Is the deflection reversible?

In order to verify that the deflection of the suspended parts of the fibrils was reversible, the following experiment was performed. For example, a fibril of 155 nm in diameter lying over a hole with suspended length 3.88 μm was imaged. The loading force was increased and then decreased back to approximately the original value. The parameters and results are shown in **Table 6-1**. It can be seen that for this filament the deflection was reversible and increased with increasing loading force.

Table 6-1 The reversible indentation of a FF nanotube over a hole under the loading force of AFM tip.

Loading force F (nN)	Indention δ (nm)	E_{bending} (GPa)
21.5	155	1.53
22.6	164	1.52
24.7	177	1.54
26.8	190	1.55
21.9	162	1.49

A fibril of 155 nm in diameter lying over a hole with suspended length 3.88 μm was imaged. The loading force was increased from 21.5 nN to 26.8 nN and then decreased back to 21.9 nN. The indentation was increased with the loading force from 155 nm to 190 nm and then be no more than 200 nm (which is the depth of the holes of the silicon substrate). If the loading force exceeded this limit, the fibril would probably be touching and sticking to the bottom of the hole and therefore the indentation might not be reversible any more. In this particular sample above (**Table 6-1**), the loading force could not exceed 27.7 nN.

As stated in section 6.1, from the profile of a fibril over a hole with “good” deflection, the E_{bending} could be calculated. In order to calculate E and G , a fibril lying across several holes with at least three different suspended lengths was however needed (Salvetat *et al.* 1999; Kis *et al.* 2002), which was particularly difficult to obtain.

Obtaining E and G

An example of a fibril lying across five holes of the silicon grid is displayed in **Figure 6-5**. As can be observed, the fibril has different suspended lengths over each hole. For this fibril, its length also exceeds the maximum scan size.

Using the height determined from the profile of the cross section as the diameter D , E_{bending} was obtained from **Equation 6-2**. The graph of $1/E_{\text{bending}}$ against $1/L^2$ for this fibril is displayed in **Figure 6-6**. From **Equation 6-3**, assuming the geometry of the cross section was constant, the Young’s modulus E was determined as 27 ± 4 GPa and the shear modulus G as 0.21 ± 0.03 GPa (Niu *et al.* 2007).

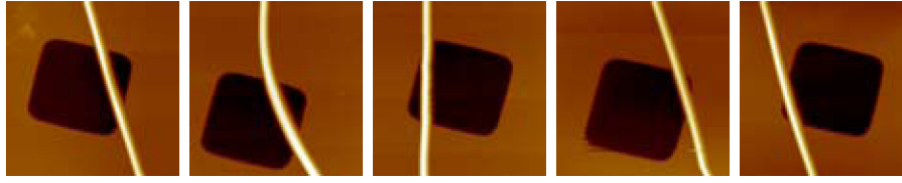


Figure 6-5 AFM images of a single FF nanotube on a silicon grid. One fibril lying across five holes of silicon grid, consequently with different suspended lengths L . The diameter of the fibril was 236 nm and the loading force was 86.7 nN. The size of each image is $10\ \mu\text{m} \times 10\ \mu\text{m}$ and the Z-range is 704 nm (figure adapted from Niu *et al.* 2007).

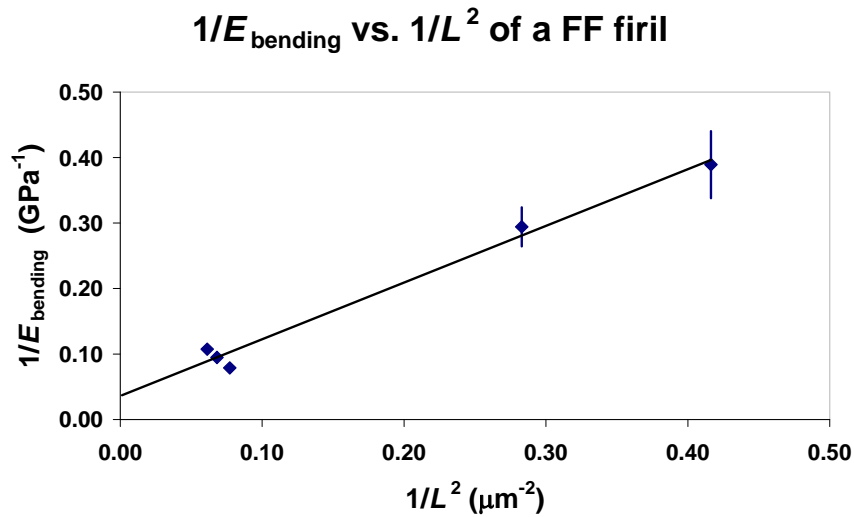


Figure 6-6 The graph of $1/E_{\text{bending}}$ against $1/L^2$ of the fibril in **Figure 6-5**. The error bars of the three left points are within the marker size.

From direct force measurement (indentation experiments) in a previous AFM study, the Young's modulus of FF nanotubes was determined to be 19 GPa (Kol *et al.* 2005). The result obtained using bending beam model therefore agreed with the result from direct force measurement. The difficulty of using direct force measurements however, is the need to align the AFM tip on the middle of a single

fibril. The bending beam model avoids this serious difficulty and also allows the shear modulus to be obtained.

The result showed that G is only $\sim 1\text{-}3\%$ of E . For ordinary materials which are homogeneous and linearly elastic, G is typically 0.3 to 0.5 times of E (Gere 1991). The low G/E ratio therefore suggests that FF nanotubes are anisotropic materials and the FF peptides are more strongly bound in the longitudinal direction than the axial direction. In FF nanotubes, there are hydrogen bonds and aromatic stacking interactions between the individual FF peptides. It is highly possible that hydrogen bonds contribute more in the longitudinal direction while aromatic stacking interactions contribute more in the axial direction (Görbitz 2006).

Determination of D effects the resulting E and G

For the bending beam model, the boundary conditions are critical. The fibrils studied were usually several times longer than the size of the holes of the silicon grid; the position of the fibrils remained the same through AFM operation, so we could assume a fibril suspended on a hole was clamped at the two ends. The main source of experimental error therefore comes from the determination of diameter D , because the bending modulus E_{bending} is related to the fourth power of D (see section 6.1.1). If the cross section of the fibril is a filled circular area, using the height determined from the profile of the cross section as the diameter D , the Young's modulus E is 27 ± 4 GPa and the shear modulus G is 0.21 ± 0.03 GPa. Using the width at the half height as diameter D (see section 2.1.3), E is 3.6 ± 0.6 GPa and G is 0.08 ± 0.01 GPa. However, the FF nanotubes are actually hollow tubes (Reches and Gazit 2003; Song *et al.* 2004; also see section 1.3.3), but the inner diameter could not be obtained from AFM imaging. If the cross section of

the fibril is a hollow circular area, assuming the inner diameter D_i is 70% of the outer diameter D_o (Song *et al.* 2004), using the width at the half height as outer diameter D_o , the resulting E is 4.7 ± 0.7 GPa and G is 0.15 ± 0.02 GPa, which does not change the order of magnitude.

If as stated in Kol's paper (2005), the diameter of the cross section (from ~150 nm to ~300 nm) does not have effect on the Young's modulus of FF nanotubes, the Young's modulus obtained from any single one of FF nanotubes using this bending beam method represents the Young's modulus of all the FF nanotubes. However, as described in section 4.4, this conclusion could not be drawn before all diameters (from under 150 nm to more than 300 nm) have been investigated. The bending beam method has the potential to be used to investigate the relationship between the diameter of the cross section and the Young's modulus, provided substrates with different sizes and/or depths of cavities are to be used.

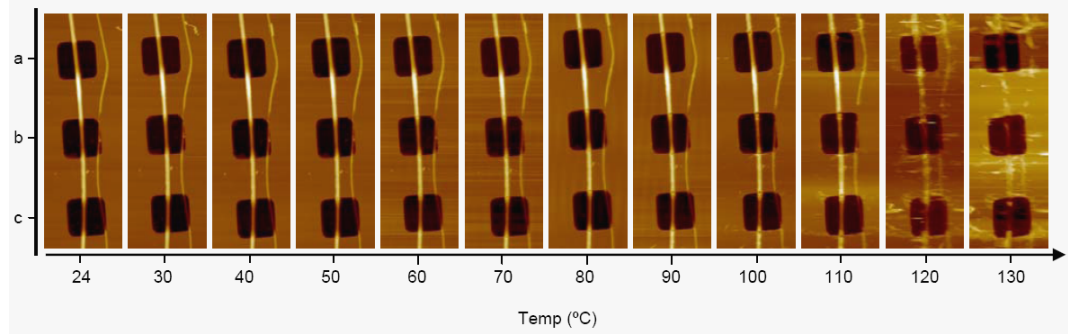
6.3.2 Effect of Temperature on the Elasticity of FF

For temperature studies, samples were placed onto the stage of EnviroScope AFM (Digital Instruments) and initially imaged at room temperature. The temperature was then increased from 30 °C to 130 °C with increments of 10 °C. Following each temperature increase the system was allowed to equilibrate for 5 minutes before imaging commenced (see section 2.1.2 for the details).

A sequence of images of the same two fibrils from room temperature (24 °C) to 130 °C is displayed (Figure 6-7 (i)). There was no visible change on the morphology of the fibrils at temperatures up to 100 °C. Higher temperatures caused the fibrils to begin to lose their structural integrity (Sedman *et al.* 2006; Kol *et al.* 2005). The three lines on Figure 6-7 (ii) show the value of E_{bending} for the

three holes (a, b, c) correspondingly of the left fibril on **Figure 6-7 (i)** at temperatures from 24 °C to 100 °C. The value of E_{bending} gradually decreased ~30% over this temperature range.

(i)



(ii)

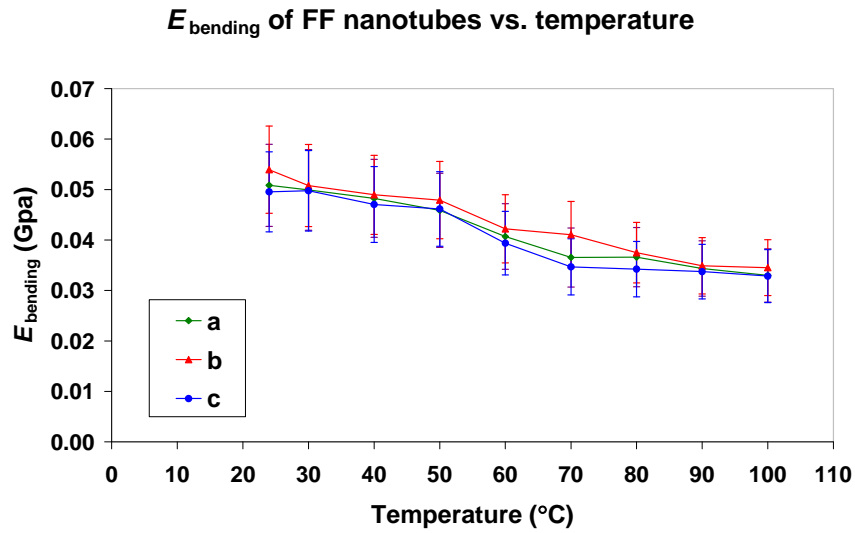


Figure 6-7 AFM images of FF nanotubes at different temperatures. (i) A sequence of images of the same two fibrils at the temperature from 24 to 130 °C. The size of each image is 30 μm (height) \times 10 μm (width). The Z-range of all the images in (i) is $1.18 \pm 0.08 \mu\text{m}$. Three lines on (ii) show the E_{bending} at three holes (a, b, c) correspondingly to the left fibril on (i) at temperature from 24 to 100 °C (Niu *et al.* 2007).

A previous high-resolution scanning electron microscope (HRSEM) study showed that the FF nanotubes kept the same morphology at temperatures up to 150 °C (Adler-Abramovich *et al.* 2006). In previous AFM study however, Sedman and co-workers (2006) showed that during *in situ* heating experiments FF nanotubes kept their wall integrity at temperatures up to 100 °C. On increasing the temperature further to 150 °C, the nanotubes lost spatial volume. They suggested that this was possibly because of the loss of water from the FF nanotubes, and that the elevated temperature made the nanotubes more deformable as they became distorted by the AFM probe as part of the imaging process. Time-of-flight secondary ion mass spectrometry (ToF-SIMS) analysis suggested that at temperatures at and above 150 °C, the loss in mass and apparent degradation in the nanotubes morphology is due to the loss of phenylalanine (Sedman *et al.* 2006).

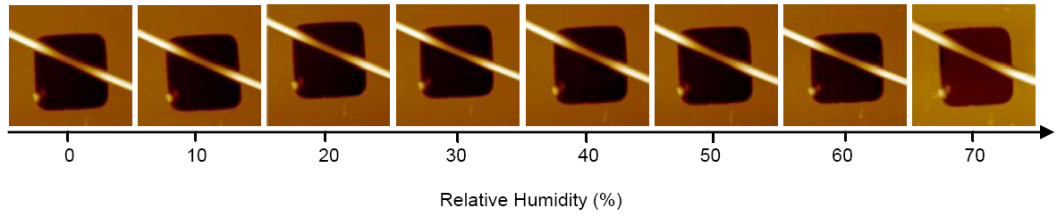
The present study showed that the value of E_{bending} gradually decreased ~30% at temperature from 24 °C to 100 °C. A possible reason could be that the increase in temperature increases the movement of FF peptides within the FF nanotube, which decreases the strength of the interactions between them. This, in-turn results in a decrease in E and G , also E_{bending} . However, since the decrease of E_{bending} was only ~30% at temperature from 24 °C to 100 °C, without changing the order of magnitude, the conclusion could be drawn that the elasticity as well as morphology of FF nanotubes remained stable (on the experimental time scale) as the temperature was increased from room temperature (24 °C) up to 100 °C. This is consistent with the previous studies (Adler-Abramovich *et al.* 2006; Sedman *et al.* 2006).

6.3.3 Effect of Humidity on the Elasticity of FF Nanotubes

In a similar manner to the temperature studies described in section 6.3.2, a study of the relation between the elasticity of FF nanotubes and humidity was carried out. The relative humidity was first decreased to near 0, and then increased to 70% in increments of 10%. Following each humidity increase the system was allowed to equilibrate for 5 minutes (details see section 2.1.2).

A sequence of images of the same fibril lying across a hole at humidities from 0 to 70% RH is displayed (**Figure 6-8 (i)**). The E_{bending} of three different fibrils in three different humidity experiments is also displayed (**Figure 6-8 (ii)**). There was no visible change in morphology of the fibrils from 0 to 70% RH. Nor was there an obvious relation between the E_{bending} and the relative humidity. For each fibril, the maximum difference of the E_{bending} at different relative humidity was less than 50%.

(i)



(ii)

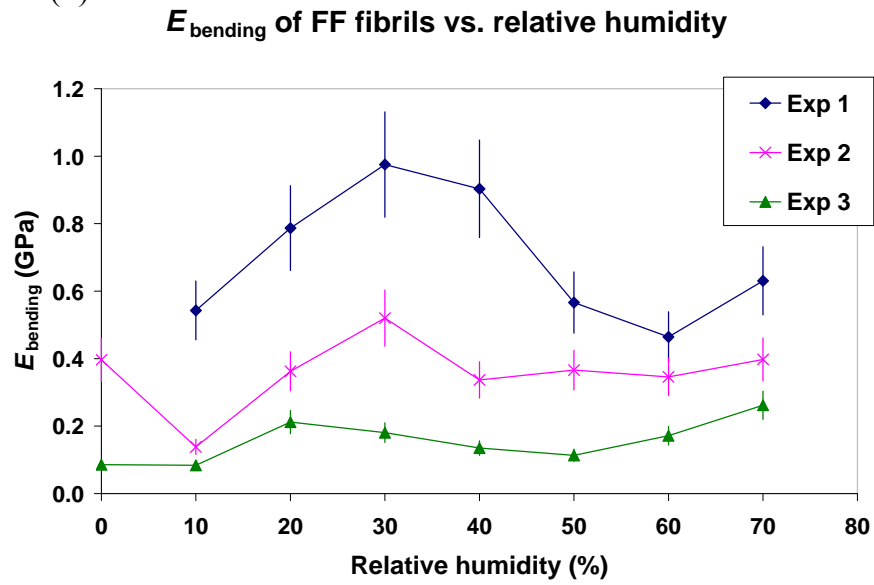


Figure 6-8 AFM images of FF nanotubes at different relative humidities. (i) A sequence of images of a same fibril lying across a hole at relative humidities from 0% to 70%. The size of each image is $10\ \mu\text{m} \times 10\ \mu\text{m}$. The Z-range of all the images in (i) is $1.07 \pm 0.02\ \mu\text{m}$. (ii) E_{bending} of three different fibrils in three different humidity experiments (Niu *et al.* 2007).

6.4 Conclusion

A suspended beam configuration at the nanoscale can be produced when a protein nanotube is placed over a cavity within an underlying substrate. The elastic deformation of the suspended part of this nanoscale beam depends on the dimension of this beam, the suspended length, the loading force on the beam and also the elasticity of this beam (Gere 1991). When imaging a protein nanotube over a cavity using AFM in contact mode, the AFM probe applies a certain loading force on the nanotube; at the same time information on the dimension of the nanotube and the suspended length can be obtained from AFM images. Therefore, the elasticity of the protein nanotube can be obtained (Salvetat *et al.* 1999; Kis *et al.* 2002; Niu *et al.* 2007). In this chapter, the work of applying bending beam model to FF nanotubes has been presented.

Using bending beam model, the Young's modulus 27 ± 4 GPa and the shear modulus 0.21 ± 0.03 GPa of FF fibrils were obtained. It has also been shown that FF nanotubes retained their rigidity at temperatures from room temperature up to 100 °C, and also relative humidities from 0 to 70%. This study has therefore provided a better understanding of the structure and properties of FF nanotubes. If FF nanotubes are to be used as biomaterials, such as scaffolds for metal wires and nanoelectromechanics (see section 1.3.3.3 for the applications of FF nanotubes), the knowledge of how their elastic properties vary with simple parameters such as temperature and humidity is essential.

For the type of investigation performed within this chapter, the bending beam method avoids difficulties with aligning the AFM tip on the middle of a single

nanotube, as is needed in direct force measurement (Kol *et al.* 2005). It also allows the shear modulus to be obtained along with the Young's modulus. The bending beam method also can provide a way to study the relation between the elasticity and the dimension of the nanotubes, as well as the environmental conditions (such as temperature, humidity and solution). However, the bending beam method is only suitable for protein nanotubes with relatively high Young's modulus.

Salvetat and co-workers (1995) applied bending beam model to single-walled carbon nanotube and obtained the Young's modulus ~ 1 TPa; Kis (2002), Kasas (2004) and co-workers applied the bending beam model to microtubules and suggested that the Young's modulus was ~ 2 GPa, with a lower limit of 100 MPa. The Young's modulus of FF fibrils obtained in the presented study was 27 GPa. Neither the attempt to apply bending beam model to $\beta 2$ -microglobulin fibrils nor to *Salmonella* flagellar filaments was successful. These protein nanotubes broke over the cavities of gold substrate under the forces associated with sample preparation and/or applied by the AFM tip during imaging. From other elasticity studies presented in the previous chapters (**chapter 4** and **5**) and in the literature (Trachtenberg and Hammel 1992; Gosal *et al.* 2005), these protein nanotubes have the Young's modulus on the order of 10^1 to 10^2 MPa. From all these available data, it seems that the lower limit of the Young's modulus of nanotubes or fibrils that the bending beam model can be applied to is on the order of 1 GPa.

Chapter 7 Final Conclusions: AFM is a Powerful Tool for Investigating the Properties of Protein Nanotubes

Protein nanotubes have a wide range of potential applications in biotechnology (see section 1.2.3, 1.3.2 and 1.3.3.3). A comprehensive understanding of their properties has therefore become a prerequisite for their use in rational materials design. In this thesis, a range of protein nanotubes have been investigated by AFM as examples to develop methods of obtaining the structural and mechanical information of protein nanotubes. In this final chapter, the methods presented in previous chapters will be compared, in addition to a summary of the protein nanotube property data obtained.

7.1 AFM Methods of Investigating Protein Nanotubes

AFM is capable of visualizing and monitoring dynamic processes. Not only could the change in morphology of protein nanotubes be visualized, but also changes in their mechanical properties were monitored as dynamic processes. For example, changes in the morphology (see section 3.2) and flexibility (see section 4.3) of lysozyme fibrils during fibrillization were investigated. As another example, the morphologies and the elasticities of FF nanotubes were monitored as temperatures were increased from room temperature to 100 °C (see section 6.3.2).

Chapters 4 to 6 describe a range of different methods to obtain the mechanical properties of protein nanotubes. Historically, the indentation method has been used to obtain the elastic properties of samples using AFM. The indentation method is based on pressing the AFM probe into the nanotube sample surface, and the contact region of the resulting force-versus-distance curves used to provide quantitative information on its elastic properties. However, this method was not suitable for most of the protein nanotubes analysed within this thesis. For instance, the diameters of the protein nanotubes investigated in this thesis were typically in the range of 5-200 nm. Commonly used silicon nitride AFM probes have a nominal tip radius of 20 nm (manufacturer's data; Veeco Probes, Camarillo, CA, USA; also see section 2.1.2). Practically it was therefore difficult to accurately locate the tip onto the centre of a protein nanotube. Even if possible, a small uncertainty in location can result in a significant error in calculating the elasticity of the protein nanotubes (Sun *et al.* 2004). In addition, since the protein nanotubes are soft and thin, the underlying substrate modulus may interfere with the force-versus-distance curves, therefore interfere with the resulting elasticity of the sample obtained by indentation method. Active indentation into the protein nanotubes may also break the stress-strain linearity of the protein nanotubes. Therefore, alternative AFM methods needed to be developed/utilized to obtain the mechanical properties of protein nanotubes under investigation within this thesis.

The persistence length method, adhesive interaction method and bending beam method were described and utilized within chapters 4-6. All of these methods had the ability to investigate relationships between the elastic properties of protein nanotubes and other factors, such as the solution environment (section 4.2 and 5.2),

substrate (section 4.2), temperature (section 6.3.2) and humidity (section 6.3.3). However, each method was found only to be suitable for protein nanotubes with elasticities within a certain range. For example, the bending beam method was found to be suitable for protein nanotubes with Young's moduli above 1 GPa. The persistence length method was found to be suitable for protein nanotubes with Young's moduli on the order of 10^1 to 10^2 MPa. Although, theoretically the adhesive interaction method was suitable for protein nanotubes with a wider range of Young's moduli, it required the protein nanotubes to be immobilised onto the substrate surface in liquid.

7.2 The Mechanical Properties of Protein Nanotubes

The protein nanotubes investigated by AFM in this thesis included *Salmonella* flagellar filaments, lysozyme fibrils and FF nanotubes. *Salmonella* flagellar filaments were found to have a Young's modulus of 22 ± 4 MPa (from the persistence length method) or from 7.2 MPa to 20.5 MPa (from the adhesive interaction method). Lysozyme fibrils of different assembly levels were found to have an average Young's modulus 3.3 GPa (from persistence length method). FF nanotubes were found to have a Young's modulus 27 ± 4 GPa (from the bending beam method).

The Young's modulus of a range of materials (Alonso and Goldmann 2003) is shown in **Figure 7-1**. Putting the presented results in this thesis onto this Young's modulus scale (shown by blue arrows in **Figure 7-1**), provides us better idea when it comes to rational materials design. All of the investigated protein nanotube structures had Young's moduli lying between that of gelatin and bone (**Figure 7-1**). This strongly highlights their potential, in terms of mechanical properties, for a

range of applications including drug-delivery systems, tissue-engineering scaffolds, 3D cell culture and templating. (see section 1.2.3, 1.3.2 and 1.3.3.3).

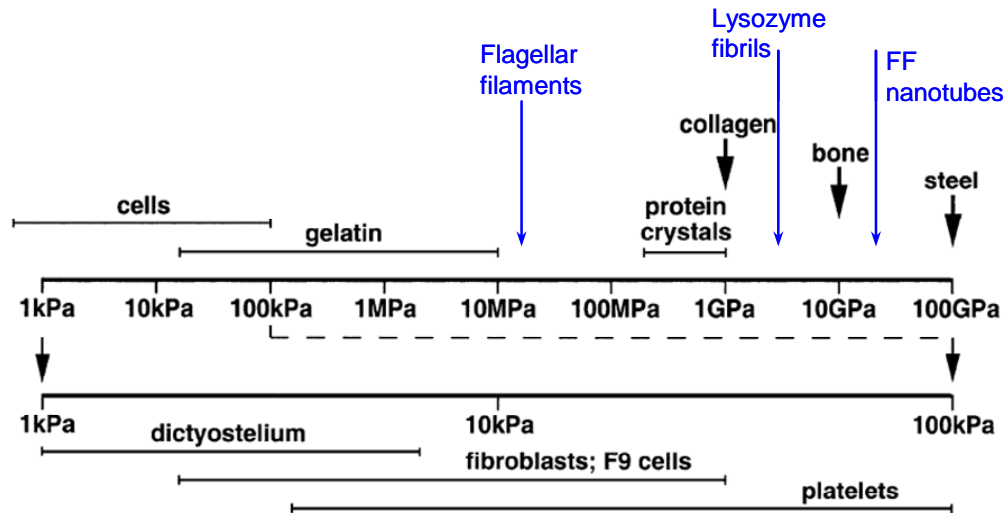


Figure 7-1 Young's modulus of different materials. The diagram shows a spectrum from very hard to very soft materials: steel > bone > collagen > protein crystals > gelatin > rubber > cells (figure adapted from Alonso and Goldmann 2003).

7.3 Future Directions

As summarised in section 7.2, the mechanical properties of three different protein nanotubes have been putting onto the Yong's modulus scale of materials. In future, if a database of mechanical properties of protein nanotubes could be built up using the AFM methods developed and utilized within this thesis, the development of the applications of protein nanotubes will be well accelerated, as the right protein nanotubes will be utilized for the right applications.

As accessories of the main aim of this thesis, which has been summarised in section 7.1 and 7.2, some of the results also inspired other directions of study. For instance, the circular structure of lysozyme fibrils were observed at the later stage of fibrillization (see section 3.2.4) without the need of high hydrostatic pressure nor the addition of organic solvents (Jasen 2004; Grudzielanek et al. 2005). Further and more in depth investigation into this matter may provide better understanding on the fibrillization mechanism of amyloid fibrils, which may be useful for understanding the amyloid related diseases and manipulating fibrillization for applications.

References

- Adami, R.; Choquet, D.; Grazi, E., Rhodamine phalloidin F-actin - Critical concentration versus tensile strength. *European Journal of Biochemistry* **1999**, 263, (1), 270-275.
- Adler-Abramovich, L.; Reches, M.; Sedman, V. L.; Allen, S.; Tendler, S. J. B.; Gazit, E., Thermal and chemical stability of diphenylalanine peptide nanotubes: Implications for nanotechnological applications. *Langmuir* **2006**, 22, (3), 1313-1320.
- Allen, S.; Chen, X. Y.; Davies, J.; Davies, M. C.; Dawkes, A. C.; Edwards, J. C.; Roberts, C. J.; Sefton, J.; Tendler, S. J. B.; Williams, P. M., Detection of antigen-antibody binding events with the atomic force microscope. *Biochemistry* **1997**, 36, (24), 7457-7463.
- Allison, D. P.; Hinterdorfer, P.; Han, W. H., Biomolecular force measurements and the atomic force microscope. *Current Opinion in Biotechnology* **2002**, 13, (1), 47-51.
- Ban, T.; Yamaguchi, K.; Goto, Y., Direct observation of amyloid fibril growth, propagation, and adaptation. *Accounts of Chemical Research* **2006**, 39, (9), 663-670.
- Baumann, C. G.; Smith, S. B.; Bloomfield, V. A.; Bustamante, C., Ionic effects on the elasticity of single DNA molecules. *Proceedings of the National Academy of Sciences of the United States of America* **1997**, 94, (12), 6185-6190.
- Berg, H. C., The rotary motor of bacterial flagella. *Annual Review of Biochemistry* **2003**, 72, 19-54.

Berry, R. M.; Armitage, J. P., The bacterial flagella motor. *Advances in Microbial Physiology*, **1999**, 41, 291-337.

Binnig, G.; Quate, C. F.; Gerber, C., Atomic Force Microscope. *Physical Review Letters* **1986**, 56, (9), 930-933.

Blair, D. F., Flagellar movement driven by proton translocation. *Febs Letters* **2003**, 545, (1), 86-95.

Bong, D. T.; Clark, T. D.; Granja, J. R.; Ghadiri, M. R., Self-assembling organic nanotubes. *Angewandte Chemie-International Edition* **2001**, 40, (6), 988-1011.

Bong, D. T.; Ghadiri, M. R., Self-assembling cyclic peptide cylinders as nuclei for crystal engineering. *Angewandte Chemie-International Edition* **2001**, 40, (11), 2163-2166.

Bottomley, L. A.; Coury, J. E.; First, P. N., Scanning probe microscopy. *Analytical Chemistry* **1996**, 68, (12), R185-R230.

Bowen, W. R.; Lovitt, R. W.; Wright, C. J., Application of atomic force microscopy to the study of micromechanical properties of biological materials. *Biotechnology Letters* **2000**, 22, (11), 893-903.

Butt, H. J.; Cappella, B.; Kappl, M., Force measurements with the atomic force microscope: Technique, interpretation and applications. *Surface Science Reports* **2005**, 59, (1-6), 1-152.

Cappella, B.; Dietler, G., Force-distance curves by atomic force microscopy. *Surface Science Reports* **1999**, 34, 1-3.

- Carrion-Vazquez, M.; Oberhauser, A. F.; Fisher, T. E.; Marszalek, P. E.; Li, H. B.; Fernandez, J. M., Mechanical design of proteins-studied by single-molecule force spectroscopy and protein engineering. *Progress in Biophysics & Molecular Biology* **2000**, 74, (1-2), 63-91.
- Chamberlain, A. K.; MacPhee, C. E.; Zurdo, J.; Morozova-Roche, L. A.; Hill, H. A. O.; Dobson, C. M.; Davis, J. J., Ultrastructural organization of amyloid fibrils by atomic force microscopy. *Biophysical Journal* **2000**, 79, (6), 3282-3293.
- Chen, R. J.; Bangsaruntip, S.; Drouvalakis, K. A.; Kam, N. W. S.; Shim, M.; Li, Y. M.; Kim, W.; Utz, P. J.; Dai, H. J., Noncovalent functionalization of carbon nanotubes for highly specific electronic biosensors. *Proceedings of the National Academy of Sciences of the United States of America* **2003**, 100, (9), 4984-4989.
- Chiti, F.; Dobson, C. M., Protein misfolding, functional amyloid, and human disease. *Annual Review of Biochemistry* **2006**, 75, 333-366.
- Dammer, U.; Hegner, M.; Anselmetti, D.; Wagner, P.; Dreier, M.; Huber, W.; Guntherodt, H. J., Specific antigen/antibody interactions measured by force microscopy. *Biophysical Journal* **1996**, 70, (5), 2437-2441.
- Dammer, Y.; Hegner, M.; Anselmetti, D.; Wagner, P.; Dreier, M.; Huber, W.; Guntherodt, H. J., Specific antigen/antibody interactions measured by force microscopy. *Biophysical Journal* **1996**, 70, (5), 2437-2441.
- Djalali, R.; Chen, Y. F.; Matsui, H., Au nanocrystal growth on nanotubes controlled by conformations and charges of sequenced peptide templates. *Journal of the American Chemical Society* **2003**, 125, (19), 5873-5879.

Dobson, C. M., Protein misfolding, evolution and disease. *Trends in Biochemical Sciences* **1999**, 24, (9), 329-332.

Dobson, C. M.; Sali, A.; Karplus, M., Protein folding: A perspective from theory and experiment. *Angewandte Chemie-International Edition* **1998**, 37, (7), 868-893.

Dufrene, Y. F., Atomic force microscopy, a powerful tool in microbiology. *Journal of Bacteriology* **2002**, 184, (19), 5205-5213.

Dupres, V.; Verbelen, C.; Dufrene, Y. F., Probing molecular recognition sites on biosurfaces using AFM. *Biomaterials* **2007**, 28, (15), 2393-2402.

Ebbesen, T. W.; Ajayan, P. M., Large-scale Synthesis of Carbon Nanotubes. *Nature* **1992**, 358, (6383), 220-222.

Engel, A.; Muller, D. J., Observing single biomolecules at work with the atomic force microscope. *Nature Structural Biology* **2000**, 7, (9), 715-718.

Fan, F.; Ohnishi, K.; Francis, N. R.; Macnab, R. M., The FliP and FliR proteins of *Salmonella typhimurium*, putative components of the type III flagellar export apparatus, are located in the flagellar basal body. *Molecular Microbiology* **1997**, 26, (5), 1035-1046.

Fennimore, A. M.; Yuzvinsky, T. D.; Han, W. Q.; Fuhrer, M. S.; Cumings, J.; Zettl, A., Rotational actuators based on carbon nanotubes. *Nature* **2003**, 424, (6947), 408-410.

Fisher, T. E.; Marszalek, P. E.; Oberhauser, A. F.; Carrion-Vazquez, M.; Fernandez, J. M., The micro-mechanics of single molecules studied with atomic force microscopy. *Journal of*

Physiology-London **1999**, 520, (1), 5-14.

Fisher, T. E.; Oberhauser, A. F.; CarrionVazquez, M.; Marszalek, P. E.; Fernandez, J. M., The study of protein mechanics with the atomic force microscope (vol 24, pg 379, 1999). *Trends in Biochemical Sciences* **2000**, 25, (1), 6-6.

Florin, E. L.; Moy, V. T.; Gaub, H. E., Adhesion Forces between Individual Ligand-receptor Pairs. *Science* **1994**, 264, (5157), 415-417.

Friedsam, C.; Seitz, M.; Gaub, H. E., Investigation of polyelectrolyte desorption by single molecule force spectroscopy. *Journal of Physics-Condensed Matter* **2004**, 16, (26), S2369-S2382.

Fukasaku, K.; Takeda, K.; Shiraishi, K., First-principles study on electronic structures of protein nanotubes. *Journal of the Physical Society of Japan* **1998**, 67, (11), 3751-3760.

Gao, X. Y.; Matsui, H., Peptide-based nanotubes and their applications in bionanotechnology. *Advanced Materials* **2005**, 17, (17), 2037-2050.

Gazit, E., A possible role for pi-stacking in the self-assembly of amyloid fibrils. *Faseb Journal* **2002**, 16, (1), 77-83.

Gere, J. M.; Timoshenko, S. P., *Mechanics of Materials*. Third SI ed.; Chapman and Hall, London: 1991.

Ghadiri, M. R.; Granja, J. R.; Milligan, R. A.; McRee, D. E.; Khazanovich, N., Self-assembling Organic Nanotubes Based on a Cyclic Peptide Architecture. *Nature* **1993**, 366, (6453), 324-327.

- Goldsbury, C.; Frey, P.; Olivieri, V.; Aebi, U.; Muller, S. A., Multiple assembly pathways underlie amyloid-beta fibril polymorphisms. *Journal of Molecular Biology* **2005**, 352, (2), 282-298.
- Gorbitz, C. H., The structure of nanotubes formed by diphenylalanine, the core recognition motif of Alzheimer's beta-amyloid polypeptide. *Chemical Communications* **2006**, (22), 2332-2334.
- Gras, S. L., Amyloid fibrils: From disease to design. New biomaterial applications for self-assembling cross-beta fibrils. *Australian Journal of Chemistry* **2007**, 60, (5), 333-342.
- Gras, S. L., Protein misfolding: a route to new nanomaterials. *Advanced Powder Technology* **2007**, 18, (6), 699-705.
- Greig, L. M.; Philp, D., Applying biological principles to the assembly and selection of synthetic superstructures. *Chemical Society Reviews* **2001**, 30, (5), 287-302.
- Grimbergen, J. A.; Visscher, K.; Demesquita, D. S. G.; Brakenhoff, G. J., Isolation of Single Yest-cells by Optical Trapping. *Yeast* **1993**, 9, (7), 723-732.
- Guo, T.; Nikolaev, P.; Rinzler, A. G.; Tomanek, D.; Colbert, D. T.; Smalley, R. E., Self-assembly of Tubular Fullerenes. *Journal of Physical Chemistry* **1995 (a)**, 99, (27), 10694-10697.
- Guo, T.; Nikolaev, P.; Thess, A.; Colbert, D. T.; Smalley, R. E., Catalytic Growth of Single-walled Nanotubes by Laser Vaporization. *Chemical Physics Letters* **1995 (b)**, 243, (1-2), 49-54.

Hansma, H. G.; Bezanilla, M.; Zenhausern, F.; Adrian, M.; Sinsheimer, R. L., Atomic Force Microscopy of DNA in Aqueous-Solutions. *Nucleic Acids Research* **1993**, 21, (3), 505-512.

Hansma, H. G.; Sinsheimer, R. L.; Li, M. Q.; Hansma, P. K., Atomic Force Microscopy of Single-stranded and Double-stranded DNA. *Nucleic Acids Research* **1992**, 20, (14), 3585-3590.

Harata, K.; Muraki, M.; Jigami, Y., Role of ARG115 in the Catalytic Action of Human Lysozyme – X-Ray Structure of HIS115 and GLU115 and Glu115 Mutants. *Journal of Molecular Biology* **1993**, 233, (3), 524-535.

Harper, J. D.; Lansbury, P. T., Models of amyloid seeding in Alzheimer's disease and scrapie: Mechanistic truths and physiological consequences of the time-dependent solubility of amyloid proteins. *Annual Review of Biochemistry* **1997**, 66, 385-407.

Heinz, W. F.; Hoh, J. H., Relative surface charge density mapping with the atomic force microscope. *Biophysical Journal* **1999**, 76, (1), 528-538.

Hinterdorfer, P.; Baumgartner, W.; Gruber, H. J.; Schilcher, K.; Schindler, H., Detection and localization of individual antibody-antigen recognition events by atomic force microscopy. *Proceedings of the National Academy of Sciences of the United States of America* **1996**, 93, (8), 3477-3481.

Homma, M.; Iino, T., Locations of Hook-associated Proteins in Flagellar Structures of *Salmonella typhimurium*. *Journal of Bacteriology* **1985**, 162, (1), 183-189.

Inaka, K.; Kuroki, R.; Kikuchi, M.; Matsushima, M., Crystal-structures of the Apomutant and

Holomutant Human Lysozymes with an Introduced Ca^{2+} Binding-site. *Journal of Biological Chemistry* **1991**, 266, (31), 20666-20671.

Israelachvili, J. N., *Intermolecular and Surface Forces*. 2nd ed.; Academic Press: San Diego, CA, USA, 1992.

Jansen, R.; Dzwolak, W.; Winter, R., Amyloidogenic self-assembly of insulin aggregates probed by high resolution atomic force microscopy. *Biophysical Journal* **2005**, 88, (2), 1344-1353.

Jansen, R.; Grudzielanek, S.; Dzwolak, W.; Winter, R., High pressure promotes circularly shaped insulin amyloid. *Journal of Molecular Biology* **2004**, 338, (2), 203-206.

Kamiya, R.; Asakura, S., Flagellar Transformations at Alkaline pH. *Journal of Molecular Biology* **1976 (a)**, 108, (2), 513-518.

Kamiya, R.; Asakura, S., Helical Transformations of Salmonella Flagella in vitro. *Journal of Molecular Biology* **1976 (b)**, 106, (1), 167-186.

Khurana, R.; Ionescu-Zanetti, C.; Pope, M.; Li, J.; Nielson, L.; Ramirez-Alvarado, M.; Regan, L.; Fink, A. L.; Carter, S. A., A general model for amyloid fibril assembly based on morphological studies using atomic force microscopy. *Biophysical Journal* **2003**, 85, (2), 1135-1144.

Kis, A.; Kasas, S.; Babic, B.; Kulik, A. J.; Benoit, W.; Briggs, G. A. D.; Schonenberger, C.; Catsicas, S.; Forro, L., Nanomechanics of microtubules. *Physical Review Letters* **2002**, 89, (24), 248101.

- Kohli, P.; Martin, C. R., Smart nanotubes for biotechnology. *Current Pharmaceutical Biotechnology* **2005**, 6, (1), 35-47.
- Kol, N.; Adler-Abramovich, L.; Barlam, D.; Shneck, R. Z.; Gazit, E.; Rousso, I., Self-assembled peptide nanotubes are uniquely rigid bioinspired supramolecular structures. *Nano Letters* **2005**, 5, (7), 1343-1346.
- Krebs, M. R. H.; Wilkins, D. K., Formation and seeding of amyloid fibrils from wild-type hen lysozyme and a peptide fragment from the beta-domain. *Journal of Molecular Biology* **2000**, 300, (3), 541-549.
- Krejcová, K.; Rabisková, M., Nano- and microtubes for drugs. *Chemické Listy* **2008**, 102, (1), 35-39.
- Kubori, T.; Matsushima, Y.; Nakamura, D.; Uralil, J.; Lara-Tejero, M.; Sukhan, A.; Galan, J. E.; Aizawa, S., Supramolecular structure of the Salmonella typhimurium type III protein secretion system. *Science* **1998**, 280, (5363), 602-605.
- Kumara, M. T.; Srividya, N.; Muralidharan, S.; Tripp, B. C., Bioengineered flagella protein nanotubes with cysteine loops: Self-assembly and manipulation in an optical trap. *Nano Letters* **2006**, 6, (9), 2121-2129.
- Kumara, M. T.; Tripp, B. C.; Muralidharan, S., Self-assembly of metal nanoparticles and nanotubes on bioengineered flagella scaffolds. *Chemistry of Materials* **2007**, 19, (8), 2056-2064.
- Lee, G. U.; Kidwell, D. A.; Colton, R. J., Sensing Discrete Streptavidin Biotin Interactions with Atomic-Force Microscopy. *Langmuir* **1994**, 10, (2), 354-357.

- Li, W. Z.; Xie, S. S.; Qian, L. X.; Chang, B. H.; Zou, B. S.; Zhou, W. Y.; Zhao, R. A.; Wang, G., Large-scale synthesis of aligned carbon nanotubes. *Science* **1996**, 274, (5293), 1701-1703.
- Lyubchenko, Y. L.; Oden, P. I.; Lampner, D.; Lindsay, S. M.; Dunker, K. A., Atomic Force Microscopy of DNA and Bacteriophage in Air, Water and Propanol – the Role of Adhesion Forces. *Nucleic Acids Research* **1993**, 21, (5), 1117-1123.
- Makin, O. S.; Serpell, L. C., Structures for amyloid fibrils. *Febs Journal* **2005**, 272, (23), 5950-5961.
- Marti, O.; Elings, V.; Haugan, M.; Bracker, C. E.; Schneir, J.; Drake, B.; Gould, S. A. C.; Gurley, J.; Hellemans, L.; Shaw, K.; Weisenhorn, A. L.; Zasadzinski, J.; Hansma, P. K., Scanning Probe Microscopy of Biological Samples and Other Surfaces. *Journal of Microscopy-Oxford* **1988**, 152, 803-809.
- Melosh, N. A.; Boukai, A.; Diana, F.; Gerardot, B.; Badolato, A.; Petroff, P. M.; Heath, J. R., Ultrahigh-density nanowire lattices and circuits. *Science* **2003**, 300, (5616), 112-115.
- Merrill, E. W.; Dennison, K. A.; Sung, C., Partitioning and Diffusion of Solutes in Hydrogels of Poly (Ethylene Oxide). *Biomaterials* **1993**, 14, (15), 1117-1126.
- Mesibov, R.; Adler, J., Chemotaxis toward Amino-acids in Escherichia-coli. *Journal of Bacteriology* **1972**, 112, (1), 315.
- Minamino, T.; Macnab, R. M., Components of the Salmonella flagellar export apparatus and classification of export substrates. *Journal of Bacteriology* **1999**, 181, (5), 1388-1394.

- Modi, A.; Koratkar, N.; Lass, E.; Wei, B. Q.; Ajayan, P. M., Miniaturized gas ionization sensors using carbon nanotubes. *Nature* **2003**, 424, (6945), 171-174.
- Namba, K.; Vonderviszt, F., Molecular architecture of bacterial flagellum. *Quarterly Reviews of Biophysics* **1997**, 30, (1), 1-65.
- Niu, L. J.; Chen, X. Y.; Allen, S.; Tendler, S. J. B., Using the bending beam model to estimate the elasticity of diphenylalanine nanotubes. *Langmuir* **2007**, 23, (14), 7443-7446.
- Noy, A.; Vezenov, D. V.; Kayyem, J. F.; Meade, T. J.; Lieber, C. M., Stretching and breaking duplex DNA by chemical force microscopy. *Chemistry & Biology* **1997**, 4, (7), 519-527.
- Ohnishi, K.; Ohto, Y.; Aizawa, S. I.; Macnab, R. M.; Iino, T., FLGD Is a Scaffolding Protein Needed for Flagellar Hook Assembly in *Salmonella*-typhimurium. *Journal of Bacteriology* **1994**, 176, (8), 2272-2281.
- Okamoto, H.; Takeda, K.; Shiraishi, K., First-principles study of the electronic and molecular structure of protein nanotubes. *Physical Review B* **2001**, 64, (11).
- Perutz, M. F.; Finch, J. T.; Berriman, J.; Lesk, A., Amyloid fibers are water-filled nanotubes. *Proceedings of the National Academy of Sciences of the United States of America* **2002**, 99, (8), 5591-5595.
- Radmacher, M.; Tillmann, R. W.; Fritz, M.; Gaub, H. E., From Molecules to Cells – Imaging Soft Samples with the Atomic Force Microscop. *Science* **1992**, 257, (5078), 1900-1905.
- Ralston, J.; Larson, I.; Rutland, M. W.; Feiler, A. A.; Kleijn, M., Atomic force microscopy and direct surface force measurements - (IUPAC technical report). *Pure and Applied*

Chemistry **2005**, 77, (12), 2149-2170.

Reches, M.; Gazit, E., Casting metal nanowires within discrete self-assembled peptide nanotubes. *Science* **2003**, 300, (5619), 625-627.

Reches, M.; Gazit, E., Formation of closed-cage nanostructures by self-assembly of aromatic dipeptides. *Nano Letters* **2004**, 4, (4), 581-585.

Reich, Z.; Kapon, R.; Nevo, R.; Pilpel, Y.; Zmora, S.; Scolnik, Y., Scanning force microscopy in the applied biological sciences. *Biotechnology Advances* **2001**, 19, (6), 451-485.

Rief, M.; Gautel, M.; Oesterhelt, F.; Fernandez, J. M.; Gaub, H. E., Reversible unfolding of individual titin immunoglobulin domains by AFM. *Science* **1997**, 276, (5315), 1109-1112.

Rossell, J., Protein Immobilization for AFM. PhD Thesis, University of Nottingham, **2003**.

Salvetat, J. P.; Briggs, G. A. D.; Bonard, J. M.; Bacsá, R. R.; Kulik, A. J.; Stockli, T.; Burnham, N. A.; Forro, L., Elastic and shear moduli of single-walled carbon nanotube ropes. *Physical Review Letters* **1999**, 82, (5), 944-947.

Santos, N. C.; Castanho, M., An overview of the biophysical applications of atomic force microscopy. *Biophysical Chemistry* **2004**, 107, (2), 133-149.

Sarikaya, M.; Tamerler, C.; Jen, A. K. Y.; Schulten, K.; Baneyx, F., Molecular biomimetics: nanotechnology through biology. *Nature Materials* **2003**, 2, (9), 577-585.

Scheibel, T., Protein fibers as performance proteins: new technologies and applications. *Current Opinion in Biotechnology* **2005**, 16, (4), 427-433.

Scheibel, T.; Parthasarathy, R.; Sawicki, G.; Lin, X. M.; Jaeger, H.; Lindquist, S. L., Conducting nanowires built by controlled self-assembly of amyloid fibers and selective metal deposition. *Proceedings of the National Academy of Sciences of the United States of America* **2003**, 100, (8), 4527-4532.

Sedman, V. L.; Adler-Abramovich, L.; Allen, S.; Gazit, E.; Tendler, S. J. B., Direct observation of the release of phenylalanine from diphenylalanine nanotubes. *Journal of the American Chemical Society* **2006**, 128, (21), 6903-6908.

Seo, Y.; Jhe, W., Atomic force microscopy and spectroscopy. *Reports on Progress in Physics* **2008**, 71, (1).

Seymour, F. W. K.; Doetsch, R. N., Chemotactic Responses by Motile Bacteria. *Journal of General Microbiology* **1973**, 78, (OCT), 287-296.

Shao, Z. F.; Mou, J.; Czajkowsky, D. M.; Yang, J.; Yuan, J. Y., Biological atomic force microscopy: What is achieved and what is needed. *Advances in Physics* **1996**, 45, (1), 1-86.

Sipe, J. D.; Cohen, A. S., Review: History of the amyloid fibril. *Journal of Structural Biology* **2000**, 130, (2-3), 88-98.

Smith, J. F.; Knowles, T. P. J.; Dobson, C. M.; MacPhee, C. E.; Welland, M. E., Characterization of the nanoscale properties of individual amyloid fibrils. *Proceedings of the National Academy of Sciences of the United States of America* **2006**, 103, (43), 15806-15811.

Song, Y. J.; Challa, S. R.; Medforth, C. J.; Qiu, Y.; Watt, R. K.; Pena, D.; Miller, J. E.; van Swol, F.; Shelnutt, J. A., Synthesis of peptide-nanotube platinum-nanoparticle composites.

Chemical Communications **2004**, (9), 1044-1045.

Srigiriraju, S. V.; Powers, T. R., Continuum model for polymorphism of bacterial flagella. *Phys Rev Lett* **2005**, 94, (24), 248101.

Stark, M.; Moller, C.; Muller, D. J.; Guckenberger, R., From images to interactions: High-resolution phase imaging in tapping-mode atomic force microscopy. *Biophysical Journal* **2001**, 80, (6), 3009-3018.

Steubing, R. W.; Cheng, S.; Wright, W. H.; Numajiri, Y.; Berns, M. W., Single Beam Optical Trapping and Micro manipulation of Mammalian-cells. *Proceedings of Laser-Tissue Interaction*, **1990**, 1202, 272-280.

Sun, Y. J.; Akhremitchev, B.; Walker, G. C., Using the adhesive interaction between atomic force microscopy tips and polymer surfaces to measure the elastic modulus of compliant samples. *Langmuir* **2004**, 20, (14), 5837-5845.

Tso, W. W.; Adler, J., Negative Chemotaxis in Escherichia-coli. *Journal of Bacteriology* **1974**, 118, (2), 560-576.

Vesenska, J.; Guthold, M.; Tang, C. L.; Keller, D.; Delaine, E.; Bustamante, C., Substrate Preparation for Reliable Imaging of DNA-molecules with the Scanning Force Microscope. *Ultramicroscopy* **1992**, 42, 1243-1249.

Vinckier, A.; Gervasoni, P.; Zaugg, F.; Ziegler, U.; Lindner, P.; Groscurth, P.; Pluckthun, A.; Semenza, G., Atomic force microscopy detects changes in the interaction forces between GroEL and substrate proteins. *Biophysical Journal* **1998**, 74, (6), 3256-3263.

- Waterhouse, S. H.; Gerrard, J. A., Amyloid fibrils in bionanotechnology. *Australian Journal of Chemistry* **2004**, 57, (6), 519-523.
- Weisenhorn, A. L.; Hansma, P. K.; Albrecht, T. R.; Quate, C. F., Forces in Atomic Force Microscopy in Air and Water. *Applied Physics Letters* **1989**, 54, (26), 2651-2653.
- Weisenhorn, A. L.; Maivald, P.; Butt, H. J.; Hansma, P. K., Measuring Adhesion, Attraction, and Repulsion between Surfaces in Liquids with an Atomic Force Microscope. *Physical Review B* **1992**, 45, (19), 11226-11232.
- West, P.; Starostina, N., A Guide to AFM Image Artifacts (version 1.2). <URL: <http://www.pacificnanotech.com/afm-artifacts.html>> [accessed 10 Oct 2008]
- Williams, P. M.; Shakesheff, K. M.; Davies, M. C.; Jackson, D. E.; Roberts, C. J.; Tendler, S. J. B., Blind reconstruction of scanning probe image data. *Journal of Vacuum Science & Technology B* **1996**, 14, (2), 1557-1562.
- Woods, R. D.; Takahashi, N.; Aslam, A.; Pleass, R. J.; Aizawa, S. I.; Sockett, R. E., Bifunctional nanotube scaffolds for diverse ligands are purified simply from Escherichia coli strains coexpressing two functionalized flagellar genes. *Nano Letters* **2007**, 7, (6), 1809-1816.
- Yemini, M.; Reches, M.; Gazit, E.; Rishpon, J., Peptide nanotube-modified electrodes for enzyme-biosensor applications. *Analytical Chemistry* **2005 (a)**, 77, (16), 5155-5159.
- Yemini, M.; Reches, M.; Rishpon, J.; Gazit, E., Novel electrochemical biosensing platform using self-assembled peptide nanotubes. *Nano Letters* **2005 (b)**, 5, (1), 183-186.
- Yonekura, K.; Maki-Yonekura, S.; Namba, K., Growth mechanism of the bacterial flagellar

filament. *Research in Microbiology* **2002**, 153, (4), 191-197.

Yonekura, K.; Maki-Yonekura, S.; Namba, K., Complete atomic model of the bacterial flagellar filament by electron cryomicroscopy. *Nature* **2003**, 424, (6949), 643-650.

Zasadzinski, J. A. N.; Schneir, J.; Gurley, J.; Elings, V.; Hansma, P. K., Scanning Tunneling Microscopy of Freeze-fracture Replicas of Biomembranes. *Science* **1988**, 239, (4843), 1013-1015.

Zhang, S. G., Fabrication of novel biomaterials through molecular self-assembly. *Nature Biotechnology* **2003**, 21, (10), 1171-1178.

Zhao, X. B.; Pan, F.; Lu, J. R., Recent development of peptide self-assembly. *Progress in Natural Science* **2008**, 18, (6), 653-660.

Zhong, Z. H.; Wang, D. L.; Cui, Y.; Bockrath, M. W.; Lieber, C. M., Nanowire crossbar arrays as address decoders for integrated nanosystems. *Science* **2003**, 302, (5649), 1377-1379.

Zlatanova, J.; Lindsay, S. M.; Leuba, S. H., Single molecule force spectroscopy in biology using the atomic force microscope. *Progress in Biophysics & Molecular Biology* **2000**, 74, (1-2), 37-61.

Publication

The following article based on some of the work in this thesis was published during the course of this project.

Niu, L. J.; Chen, X. Y.; Allen, S.; Tendler, S. J. B., Using the bending beam model to estimate the elasticity of diphenylalanine nanotubes. *Langmuir* **2007**, 23, (14), 7443-7446.

Using the Bending Beam Model to Estimate the Elasticity of Diphenylalanine Nanotubes

Lijiang Niu, Xinyong Chen, Stephanie Allen, and Saul J. B. Tendler*

Laboratory of Biophysics and Surface Analysis, School of Pharmacy, The University of Nottingham, Nottingham NG7 2RD, U.K.

Received April 6, 2007. In Final Form: May 18, 2007

The core recognition motif of the amyloidogenic β -amyloid polypeptide, diphenylalanine peptide, has previously been shown to self-assemble into discrete, well-ordered, stiff nanotubes under mild conditions. The nanotubes keep the same morphology from room temperature up to 100 °C. In the presented study, we applied the bending beam model to atomic force microscopy images of diphenylalanine nanotubes suspended across cavities and obtained the Young's modulus 27 ± 4 GPa and the shear modulus 0.21 ± 0.03 GPa. We also showed that the elasticity of these nanotubes is stable within the same temperature range and at relative humidity from 0% to 70%. This study furthers our understanding of the structure and properties of these nanotubes, which are important for their potential applications in biotechnology.

Introduction

Self-assembled protein and peptide nanotubes are attractive as potential building blocks for a variety of applications, including scaffolds for tissue engineering, nanowires in microelectronics, functionalized composite materials, and drug delivery devices, not only because of their biocompatibility and chemical manipulability, but also because of their large-scale production ability and simple experimental conditions.^{1–4} An understanding of the physical properties of such nanotubes is important for applications which demand structural performance.

The diphenylalanine peptide, $\text{NH}_2\text{-Phe-Phe-COOH}$, the core motif of the β -amyloid polypeptide, efficiently self-assembles into FF fibrils under mild conditions.^{5–7} Previous studies have shown that FF fibrils are hollow, water-filled structures ranging from 50 to 1000 nm in diameter and are discrete nanotubes with no branching. Studies have also suggested that there are pores on the FF nanotube walls, which run parallel to the axis of the fibril.⁸

In the current study, the elastic properties of FF nanotubes at different temperatures and humidities have been investigated using atomic force microscopy (AFM).

Materials and Methods

Preparation of FF Fibrils. FF peptide was purchased from Sigma-Aldrich (Gillingham, Dorset, UK). Fresh stock solutions were prepared by dissolving the lyophilized peptide in 1,1,1,3,3,3-hexafluoropropan-2-ol (HFIP) (Sigma-Aldrich) at a concentration of 100 mg/mL. Peptide stock solution was diluted in double distilled (dd) H_2O to a final concentration of 2 mg/mL. An aliquot of 10 μL of the sample solution was then immediately dropped onto a UV-cleaned micropatterned silicon substrate (with holes of $5 \mu\text{m} \times 5 \mu\text{m}$ and 200 nm deep) and subsequently dried under a gentle flow of nitrogen. This protocol produced fibrils which occasionally lie over the holes of the substrate.

Atomic Force Microscopy. For elasticity measurements at room temperature, AFM images were generated using a MultiMode AFM (Digital Instruments, Veeco Metrology Group, Santa Barbara, CA) with a J-type scanner. For elasticity at elevated temperatures and modified humidities, an EnviroScope AFM (eScope AFM) (Digital Instruments) was used. This AFM has an enclosed sample chamber allowing temperature control and a humidity range of 0–80% RH. All imaging was performed in air in contact mode using V-shaped levers (Veeco Metrology Group) with nominal spring constants of 0.06 N/m (manufacturer's data). Scan rates employed were 1.0–2.0 Hz. Data was analyzed using Scanning Probe Image Processor program (Image Metrology A/S, Denmark).

For temperature studies, samples were placed onto the stage and initially imaged at room temperature. The temperature was then increased from 30 to 130 °C with increments of 10 °C. Following each temperature increase, the system was allowed to equilibrate for 5 min before imaging commenced.

In a similar manner, the relative humidity was decreased to nearly 0% and then increased to 70% with increments of 10%. Following each humidity increase, the system was allowed to equilibrate for 5 min.

Theoretical Basis

As stated, the FF fibrils occasionally lie over the holes of the silicon grid, producing a suspended-beam configuration at the nanoscale. In contact mode of AFM operation, while the AFM tip is scanning over the fibril, it applies a loading force on the fibril, which can be considered as a concentrated load midway along the suspended length of the fibril (Figure 1). The elastic deformation of the suspended part of the fibril resulting from a concentrated load can be regarded as the sum of deflections due to bending and shearing. Neglecting end effects, the deflection in the middle of the suspended part of the fibril is

$$\begin{aligned}\delta &= \delta_{\text{B}} + \delta_{\text{S}} \\ &= FL^3/192EI + f_s FL/4GA \\ &= FL^3/192E_{\text{bending}}I\end{aligned}\quad (1)$$

where δ is the deflection, δ_{B} is the deflection due to bending, δ_{S} is the deflection due to shearing; E is the Young's modulus, G is the shear modulus; F is the loading force, L is the suspended length, A is the cross-sectional area of the fibril; I is the moment of inertia of area A ($I = \pi D^4/64$ for a filled circular area with diameter D ; $I = \pi(D_o^4 - D_i^4)/64$ for a circular area with outer

* E-mail: saul.tendler@nottingham.ac.uk.

(1) Gao, X. Y.; Matsui, H. *Adv. Mater.* **2005**, *17*, 2037–2050.

(2) Scheibel, T. *Curr. Opin. Biotechnol.* **2005**, *4*, 427–433.

(3) Yemini, M.; Reches, M.; Rishpon, J.; Gazit, E. *Nano Lett.* **2005**, *1*, 183–186.

(4) Yemini, M.; Reches, M.; Gazit, E.; Rishpon, J. *Anal. Chem.* **2005**, *16*, 5155–5159.

(5) Reches, M.; Gazit, E. *Science* **2003**, *3619*, 625–627.

(6) Song, Y. J.; Challa, S. R.; Medforth, C. J.; Qiu, Y.; Watt, R. K.; Pena, D.; Miller, J. E.; van Swol, F.; Shelnutt, J. A. *Chem. Commun.* **2004**, *9*, 1044–1045.

(7) Gazit, E. *FASEB J.* **2002**, *1*, 77–83.

(8) Gorbitz, C. H. *Chem. Commun.* **2006**, *22*, 2332–2334.

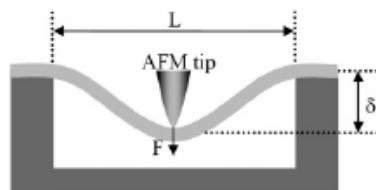


Figure 1. Schematic of the measurement. The FF fibrils occasionally lie over the holes of the silicon grid, producing a suspended beam configuration at the nanoscale. The AFM is used to apply a loading force to the fibril and to determine directly the resulting deflection.

diameter D_0 and inner diameter D_i ; f_s is the form factor for shear determined by the geometry (equal to $10/9$ for a cylindrical beam); E_{bending} is the bending modulus that corresponds to the Young's modulus that would be deduced if shear deformations were neglected^{9–11}

The deflection δ , the suspended length L , and the second moment I can be obtained from the profiles of the AFM images of the fibrils. The F is AFM loading force on the fibril, which is considered as a concentrated force midway along the suspended length of the fibril.

From eq 1

$$1/E_{\text{bending}} = 1/E + (48f_s I/GA)(1/L^2) \quad (2)$$

Hence, for a fibril lying across several holes with different suspended lengths L , assuming that the geometry of the cross section remains the same along the fibril, the Young's modulus can be obtained from the intercept of the plot of $1/E_{\text{bending}}$ versus $1/L^2$ and the shear modulus can be obtained from the gradient.

Results

Elasticity at Room Temperature. An example of a fibril lying across five holes of the silicon grid is displayed (Figure 2). As can be observed, the fibril has different suspended lengths over each hole. For this fibril, its length exceeds the maximum scan size. The deformation of the suspended parts of the fibrils was reversible and increased linearly with increasing loading force (data not shown). Using the height determined from the profile of the cross section as the diameter D , E_{bending} could be obtained from eq 1. The graph of $1/E_{\text{bending}}$ against $1/L^2$ for this fibril is displayed in Figure 2(ii). From eq 2, assuming the geometry of the cross section was constant, the Young's modulus E is 27 ± 4 GPa and the shear modulus G is 0.21 ± 0.03 GPa.

Elasticity vs Temperature. A sequence of images of the same two fibrils from room temperature to 130°C is displayed (Figure 3(i)). There was no visible change in the morphology of the fibrils at temperatures up to 100°C . Higher temperatures caused the fibrils to begin to lose their structural integrity.^{12,13} The three lines in Figure 3(ii) show the value of E_{bending} for the three holes (a, b, c) corresponding to the left fibril in Figure 3(i) at temperatures from 24 to 100°C . The value of E_{bending} gradually decreased $\sim 30\%$ over this temperature range.

Elasticity vs Humidity. A sequence of images of a same fibril lying across a hole at humidity from 0% to $70\%\text{RH}$ is

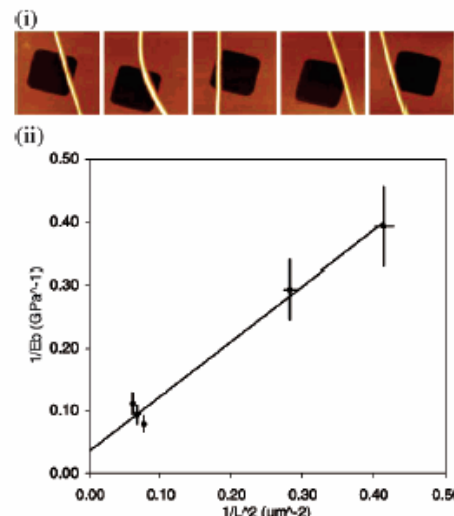


Figure 2. AFM images of a single FF nanotubes on a silicon grid. (i) One fibril lying across five holes of silicon grid, consequently with different suspended lengths L . The size of each image is $10\ \mu\text{m} \times 10\ \mu\text{m}$. From (i), the graph of $1/E_{\text{bending}}$ against $1/L^2$ of this fibril was obtained as shown in (ii).

displayed (Figure 4(i)). The E_{bending} of three different fibrils in three different elasticity vs humidity experiments is also displayed (Figure 4(ii)). There was no visible change in morphology of the fibrils from 0% to $70\%\text{RH}$, nor was there an obvious relation between the E_{bending} and the relative humidity. For each fibril, the maximum difference of the E_{bending} at different relative humidities was less than 50% .

Discussion

From direct force measurement (indentation experiments) in a previous AFM study, the Young's modulus of FF nanotubes was determined to be $19\ \text{GPa}$.¹⁴ For direct force measurement, in order to obtain the Young's modulus, the AFM tip has to be aligned at the center of a single nanotube surface and force-distance curves are acquired at the same position. The bending-beam model avoids the serious difficulty of aligning the AFM tip and also allows the shear modulus to be obtained.

For the bending-beam model, the boundary conditions are critical. The fibrils were usually several times longer than the size of the holes of the silicon grid; the position of the fibrils remained the same through AFM operation, so we could assume a fibril suspended on a hole was clamped at the two ends. The main source of experimental error or comes from the determination of diameter D , because the bending modulus E_{bending} is related to the fourth power of D . As stated in the Results section, if the cross section of the fibril is a filled circular area, using the height determined from the profile of the cross section as the diameter D , the Young's modulus E is $27 \pm 4\ \text{GPa}$ and the shear modulus G is $0.21 \pm 0.03\ \text{GPa}$. Using the width at the half-height as diameter D , E is $3.6 \pm 0.6\ \text{GPa}$ and G is $0.08 \pm 0.01\ \text{GPa}$. The FF nanotubes are actually hollow tubes, but the inner diameter could not be obtained from AFM imaging. If the cross section of the fibril is a hollow circular area, assuming the inner diameter D_i is 70% of the outer diameter D_0 , using the width at the half-height as outer diameter D_0 , the resulting E is $4.7 \pm 0.7\ \text{GPa}$ and G is $0.15 \pm 0.02\ \text{GPa}$, which does not change the order of

(9) Salvatet, J. P.; Briggs, G. A. D.; Bonard, J. M.; Bacsa, R. R.; Kulik, A. J.; Stockli, T.; Burnham, M. A.; Forno, L. *Phys. Rev. Lett.* **1999**, *5*, 944–947.

(10) Ks, A.; Kasas, S.; Babik, B.; Kulik, A. J.; Benoit, W.; Briggs, G. A. D.; Schonenberger, C.; Catsicas, S.; Forno, L. *Phys. Rev. Lett.* **2002**, *28*, 248101.

(11) Gere, J. M.; Timoshenko, S. P. *Mechanics of Materials*; Chapman and Hall: London, 1991.

(12) Adler-Abramovich, L.; Reches, M.; Sedman, V. L.; Allen, S.; Tendler, S. J. B.; Gazit, E. *Langmuir* **2006**, *3*, 1313–1320.

(13) Sedman, V. L.; Adler-Abramovich, L.; Allen, S.; Gazit, E.; Tendler, S. J. B. *J. Am. Chem. Soc.* **2006**, *21*, 6903–6908.

(14) Kol, N.; Adler-Abramovich, L.; Barlam, D.; Stueck, R. Z.; Gazit, E.; Rousso, I. *Nano Lett.* **2005**, *7*, 1343–1346.

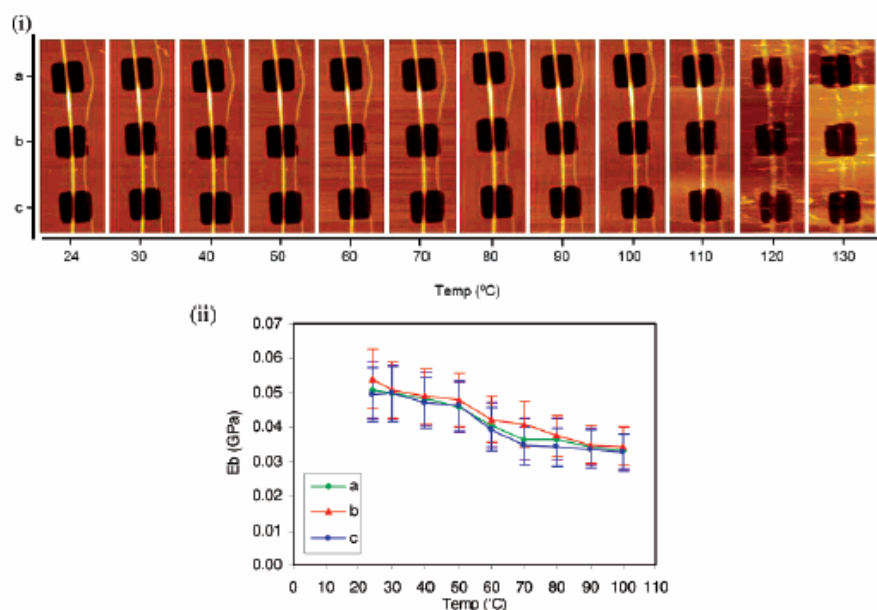


Figure 3. AFM images of FF nanotubes at different temperatures. (i) Sequence of images of the same two fibrils at the temperature from 24 to 130 °C. The size of each image is $30\ \mu\text{m}$ (height) $\times\ 10\ \mu\text{m}$ (width). Three lines on Figure 3 (ii) show the E_{bending} at three holes (a, b, c) corresponding to the left fibril on (i) at temperature from 24 to 100 °C.

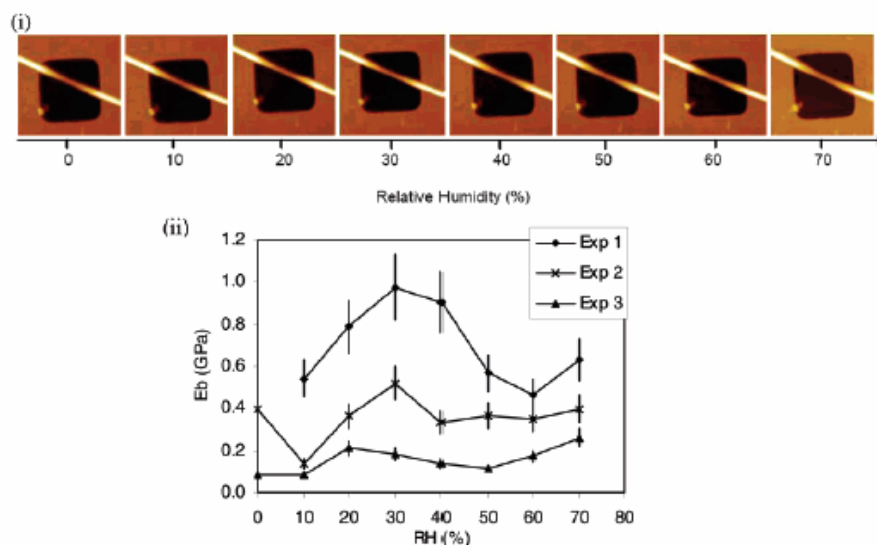


Figure 4. AFM images of FF nanotubes at different relative humidities. (i) Sequence of images of a same fibril lying across a hole at relative humidity from 0% to 70%. The size of each image is $10\ \mu\text{m} \times 10\ \mu\text{m}$. (ii) E_{bending} of three different fibrils in three different elasticity vs humidity experiments.

magnitude. Our results agreed with the result from direct force measurement.¹⁴ Our results also showed that G is only 1–3% of E . For ordinary material, which is homogeneous and linearly elastic, G is 0.3 to 0.5 times E . The low G/E ratio means FF fibrils are anisotropic materials, and the FF peptides are relatively strongly bound in the longitudinal direction compared to the axial direction. In FF fibrils, there are hydrogen bonds and aromatic stacking interactions between the individual FF peptides.⁸ It is possible that hydrogen bonds contribute more in the longitudinal direction, while aromatic stacking interactions contribute more in the axial direction.

A previous high-resolution scanning electron microscope (HRSEM) study showed that the FF nanotubes kept the same morphology at temperatures up to 150 °C.¹² In a previous AFM study, Sedman et al. showed that FF nanotubes kept the wall integrity at temperatures up to 100 °C in situ. On increasing the temperature further to 150 °C, the nanotubes lost spatial volume. They suggested that this was possibly because of the loss of water from the FF nanotubes, and that the elevated temperature made the nanotubes more deformable and they became distorted by the AFM probe as part of the imaging process.¹³ Time-of-flight secondary ion mass spectrometry (ToF-SIMS) analysis

suggested that at temperatures at and above 150 °C, the loss in mass and apparent degradation in the nanotubes morphology is due to the loss of free phenylalanine.¹³ The present AFM study showed that the elasticity as well as morphology of FF nanotubes remained stable from room temperature up to 100 °C during the experimental time scale. This consists with all the previous studies. The present study also shows that the value of E_{bending} gradually decreased $\sim 30\%$ at temperature from 24 to 100 °C. A possible reason could be that the increase in temperature increases the movement of FF peptides in the FF fibril, which decreases the strength of the hydrogen bonds and aromatic stacking interactions between them. This causes the decreasing of E and G , which results in the decrease of E_{bending} .

Conclusions

We investigated the elastic properties of FF nanotubes by applying the bending-beam model to AFM images. We obtained the Young's modulus E of 27 ± 4 GPa and the shear modulus G of 0.21 ± 0.03 GPa of FF fibrils. We also showed that FF nanotubes kept their rigidity at temperature from room temperature up to 100 °C and relative humidity from 0% to 70%. Our study provided a better understanding of the structure and properties of FF nanotubes, which are important for their potential applications in biotechnology, such as biosensors, nanoelectromechanics, and medical devices.

LA7010106